Local Magnetic Shear Control in a Tokamak via Fast-Wave Minority-Ion Current Drive: Theory and Experiments in JET

V P Bhatnagar, D F H Start, J Jacquinot, F Chaland, A Cherubini, F Porcelli.

JET Joint Undertaking, Abingdon, Oxon, OX14 3EA, UK.

ABSTRACT.

When an ion cyclotron resonance heating (ICRH) antenna array is phased ($\Delta\phi \neq 0$ or π), the excited asymmetric $k_{//}$-spectrum can drive non inductive currents by interaction of fast waves both with electrons (transit-time magnetic pumping (e-TTMP) and Landau damping (e-LD)) and ions at minority (fundamental) or harmonic cyclotron resonances depending upon the scenario. Based on earlier theories, we present a simplified description that includes the minority-ion and electron current drive effects simultaneously in a 3-D ray tracing calculation in the tokamak geometry. The experimental results of sawtooth stabilization or destabilization in JET using the minority-ion current drive scheme are presented. This scheme allows a modification of the local current density gradient (or the magnetic shear) at the $q = 1$ surface resulting in a control of sawteeth. Predictions of the above model of current drive and its effects on sawtooth period calculated in conjunction with a model of stability of internal resistive kink modes, that encompasses effects of both the fast particle pressure and the local ($q = 1$) magnetic shear, are found to be qualitatively in good agreement with experimental results. Further, we discuss results of our model of fast wave current drive scenarios of magnetic shear reversal with a view to achieving long duration high confinement regimes in the forthcoming experimental campaign of JET. Finally, we present results of minority current drive for sawtooth control in next-step devices such as International Thermonuclear Experimental Reactor (ITER).

1. INTRODUCTION.

A controlled local modification of the plasma-current density profile, the safety factor q or magnetic shear (dq/dr) in a tokamak can lead to an improvement in its performance [1]. For example, enhanced confinement in JET discharges with deep pellet injection is found to be associated with a reversal of the shear [2]. This enhancement due to pellets is inherently of short duration. Shear reversals for a long duration can be obtained by a careful combination of the fast wave electron and ion current drive effects. Also, a significant control over the sawteeth behaviour in the JET tokamak has been found to occur when the magnetic shear at the $q = 1$ surface is modified by a dipolar-current driven by ICRF in the minority-ion heating regime [3]. This could give a handle on the ejection of fast particles and hence on burn control in a reactor. The above sawtooth control may also be used to ease the ash removal in a reactor.

When an ICRH antenna array is phased ($\Delta\phi \neq 0$ or π), the excited asymmetric $k_{//}$-spectrum can drive non inductive currents by interaction of waves both with electrons and ions. Therefore, in any modeling of fast wave current drive, both (electron and ion) current drive mechanisms must be included simultaneously to correctly represent the non inductive current drive profile. We have developed a

1

model based on earlier theories to calculate, for the first time, the two effects simultaneously. These theoretical calculations are used primarily to devise potential scenarios of shear control in tokamaks both for sawtooth stablization and destabilization (shear control at $q = 1$ by minority current drive) and high confinement regimes (shear control well within $q = 1$ surface by minority current drive and taking advantage of the inherent electron current drive).

For current drive physics see a review paper by Fisch [4]. The fast waves can penetrate to the centre of a high density, high temperature reactor plasma and they are not subject to any density limits. For electron current drive, they can be used with parallel phase velocity up to the speed of light enjoying a higher efficiency (current drive efficiency $\propto v_{//}^2$) at the Landau resonance ($\omega = k_{//}v_{//}$). The ion current drive can modify the gradient of the current profile (see below) adequately for sawteeth control at modest power levels. Our e-TTMP and e-LD current drive calculations have previously been discussed in [5] and we outline them only briefly here. In this paper, we concentrate on the minority current drive physics of the calculation although the results include both mechanisms.

The minority-ion current drive was first discussed by Fisch [6]. The resonant condition $\omega - \omega_{ci} = k_{//} \cdot v_{//i}$ suggests that the sign of the driven current reverses on the two sides of the minority cyclotron layer in a tokamak when the damping is not too strong. Since the effect is local, it can be used to advantage to modify the gradient of the plasma current density especially near the $q = 1$ surface. Both theoretically and experimentally, it has been found that two different mechanism can be used to control the sawteeth [7] while allowing q on axis to drop below unity: (i) stabilization by minority fast-ion pressure and (ii) a reduction of the local ($q = 1$) magnetic shear. Note that the latter effect requires phasing of the antenna array so as to excite asymmetric $k_{//}$-spectrum. Result of the present calculation provide the e-TTMP and minority current drive (MCD) profile which form an input to another code that study the stability of resistive internal kink modes (sawtooth instability) encompassing both effects of fast-ion pressure and local magnetic shear [7]. This allows us to compare experimental results of sawtooth period with those predicted by our current drive model. The paper is organised as follows. In section 2, we present an analysis of the electron and minority ion current drive models that are integrated into a ray tracing code for calculating the current drive profiles. Experimental results of sawtooth stabilization and destabilization by minority current drive are given in Section 3 where we also present results of the sensitivity of sawtooth period on the relative position of $q = 1$ and minority cyclotron layer. In section 4, we compare theoretical results of normalized current drive efficiencies for several different minority and majority species combinations. In this section, we also calculate the fast wave current drive for a discharge presented in Section 3 and compare the experimentally observed sawtooth periods in JET under minority current drive scenarios with those predicted by the theory. In Section 5, we present potential scenarios of shear control in JET for long

2

duration high confinement regimes using fast wave minority ion and electron current drive effects. We also discuss, in this section, the results of a minority current drive scenario for sawtooth control in next-step devices such as ITER. Discussion and conclusions of this study are contained in section 6.

2. FAST-WAVE CURRENT-DRIVE MODEL.

The theory of non inductive current drive in a tokamak, generally, requires the solution of a bounce-averaged Fokker-Planck equation. Quasilinear theory can deal with the collisionless interaction of RF waves with a plasma and RF effects can be included by a quasilinear ICRF diffusion operator. This provides appropriate distribution functions from which averages of macroscopic variables can be deduced by integration and the efficiency of RF current current drive can be calculated. However, to be consistent in solving the Fokker-Planck equation, one must solve for the linear wave field using a full-wave solution in toroidal geometry for a given antenna array that is phased to provide an asymmetric $k_{//}$-spectrum. Such a spectrum is necessary for providing the asymmetry in velocity space of the RF operator responsible for current drive. The calculated directivity can then also be included in the results of current drive efficiencies.

The primary aim of the present fast-wave current drive theoretical model is to devise potential scenarios of shear control in tokamaks both for sawtooth control and high confinement regimes rather than to produce a rigorous model which are often cumbersome in their turn-around of results. Therefore, we use the ray tracing technique instead, which contains the essential physics including the effects of poloidal field on $k_{//}$. But, eigenmodes in weak damping cases are not described.

A schematic block diagram showing the layout of our code calculations is given in Fig. 1. First, we solve the phased, planar antenna-plasma coupling problem by a full-wave solution in the edge plasma region which fixes the initial conditions for ray tracing [8]. The ray tracing solution in a 3-D tokamak geometry is then carried out in the central hot plasma region where the absorption takes place. The current drive efficiencies are treated as follows: (1) The electron current drive efficiencies at each step of ray trace are calculated by analytic fits, that include the effect of electron trapping and Z_{eff} [9] to more complete Fokker Planck numerical codes. (2) To calculate the minority-ion current drive efficiencies, a flux-surface averaged ion power deposition profile is first generated with the ray tracing procedure. For the resulting power density on each flux surface, the minority ion energy distribution function is obtained by Stix model [10]. The normalized minority current drive efficiencies similar to that obtained by Fisch [6] and modified by Chiu [11], but that are more generalized in this paper, are used that take into account the back electron current, electron trapping, majority-ion rotation and Z_{eff}. Although the relative effect of

3

minority-ion trapping, when rays access different regions of the plasma cross section, is taken into account, the actual transfer of particles from non-trapped to trapped regions and the resulting increased cancellation of minority current, the so-called Ohkawa effect [12], is not included. We will present results when the cyclotron layer is located on the high-field side where this effect is less important.

2.1 Antenna Plasma Coupling and Directivity. We analyse the excitation of fast waves by an ICRH antenna array in a semi-infinite (strong damping and no reflected wave), planar (antenna length smaller than the plasma height), cold (edge) plasma model with finite width and length of an antenna element. The detail of this model has been given elsewhere [8,13] but, here we point out that analysis of this model gives (1) the radiation resistance of the antenna array, (2) the directivity, (3) asymmetric $k_{//}$-spectrum and (4) the initial conditions for starting ray tracing from a plasma region where WKB-assumptions are satisfied. These initial conditions are obtained from a partial-wave [14] analysis for an array of antennas. The directivity is defined as

$$D = \sum_{n=1}^{n} \frac{P(n) - P(-n)}{P_{tot}} \tag{1}$$

where n is the toroidal mode number. Note that this treatment allows us to include in our calculations, the phasing and directivity of the antenna array and the power coupled to the plasma from the RF generator and transmission line hardware system. A treatment of the circulating power in the current drive phasing and matching of the generator can be found elsewhere [15].

2.2 Ray Tracing. In a region, away from the fast-wave evanescence of the plasma, where the geometric optics approximation is valid, ray tracing equations are solved [8] in 3-dimensions for multispecies plasma with arbitrary density and temperature profiles. Both toroidal and poloidal components of the magnetic field and their profiles are taken into account including the variation of $k_{//}$ due to the poloidal field which is of considerable importance in damping and current drive efficiency calculations. Power absorbed by different species along the ray path is computed using a hot plasma description which contains e-TTMP and e-LD and, fundamental and second harmonic dampings. The non circular (D-shape) tokamak geometry is described analytically in terms of elongation, triangularity and Shafranov shift of the magnetic axis. In order to generate absorption and current-drive profile, we subdivide the plasma into a certain number of annular regions similar to magnetic surfaces. Starting at a flux surface, typically 90 rays are launched from several poloidal locations that encompass the excited $k_{//}$-power spectrum weighted by the square of the antenna current variation in the poloidal direction. Ray tracing is continued for multiple passes until the power left in a ray is below a desired value.

2.3 Electron Current Drive Efficiencies. At each step of the ray, the normalized current drive efficiency (see below) $\eta = (J/P_d)_n$ can be calculated by the bounce averaged Fokker-Planck theory [16]. The details of the calculation of η and the model used are given in Ref. 16. However, in order to reduce the computation time, we have found the use of an analytic fit due to Ehst [9] much more convenient. The analytic fit has been checked against the numerical results of Ref. 17 within an accuracy of $\pm$ 12% and succesfully reproduces the effects such as : (1) the current drive efficiency decreases with ξ ($= v_{ph}/v_{th}$) for low ξ, reaches a minimum at about ξ = 1 and then increases with ξ, (2) the effect of trapping reduces with decreasing inverse aspect ratio, (3) Effect of trapping is small for large values of ξ, but increases dramatically for ξ < 1 for particles on the low-field side and (4) current drive efficiency reduces with increasing Z_{eff}.

2.4 Minority-Ion Current Drive Efficiencies. The minority ion current drive calculations follow the treatment by Fisch [6] which was specialized to background ion charge of unity and no impurity species. Since there is a possibility of exploitation of several different minority scenarios such as (H)D, (H)He3, (He3)D, (D)T etc. (the minority species is enclosed in parantheses), we extend Fisch's treatment and present expressions in terms of generalized minority and majority species and in which impurity ion species and an effective plasma charge (Z_{eff}) is also included. When determining the net total current driven which must include the response of the bulk plasma (electrons and background ion species) and the effect of trapping especially those of electrons, we follow Chiu et al. [11] and Connor and Cordey [18]. The effect of trapping of heated species is also included in a simplified way.

As mentioned before, the physics of the minority ion current drive has been discussed by Fisch [6]. The minority current drive calculation is based on a modification of minority ions collision frequency (v) with background species in the velocity space. When the $k_{//}$-spectrum excited by the antenna is asymmetric, minority ions moving in one direction will gain $\perp$ energy from the wave and the minority ion total velocity increases and v decreases. These minority ions going in one direction collide less frequently as compared to minority ions going in the opposite direction and a net toroidal drift of minority ions is established. To conserve toroidal momentum, background ions drift in the opposite direction and thus a relative drift between minority and background ions is established. This relative drift depends on the variation of collision frequency [6] (in the velocity space) which is strongest when $E \approx E_c$ where E_c is the critical energy [10] and is given by

$$E_c = 16 T_e A_t \left[\frac{1}{n_e} \sum_i \frac{n_i Z_i^2}{A_i} \right]^{2/3} \tag{2}$$

where T_e is the electron temperature, A_t is the atomic mass of the minority ion, n is the density and Z is the charge. The subscript e and i refer to electrons and the

background ion species in the plasma respectively. We note that the minority current drive is optimum when $E = E_c$ and the minority ions collide with electrons and background ions roughly equally. The minority current is weaker when the relative drift is small which occurs when (a) $E \ll E_c$ i.e. minority ions collide heavily with background ions and (b) $E \gg E_c$ i.e. minority ions collide heavily with electrons. Also a higher $\perp$ energy of the minority leads to increased trapping and decreases minority ion current drive when the cyclotron layer is located on the low-field-side. Increased trapping of minority in one direction effectively increases current in the other direction (Ohkawa effect) [12] and may lead to a further reduction or possibly even a reversal of current depending upon the directivity.

Electrons are dragged collisionally both by minority and background ions that drift in opposite directions and contribute to a further modification of net total current. Electrons would have cancelled the minority current totally when $Z_h = Z_{eff}$ were it not for the trapping of electrons in the tokamak geometry. Similary the reduction of minority current, due to majority ion rotation in the opposite direction, is now further increased by electron trapping and decreases the net current driven.

Let the minority ion species drift with a velocity v_h parallel to the magnetic field and assume that the velocities of majority and impurity species are the same. If the plasma has no net parallel momentum (minority heating imparts no parallel momentum), the drift must satisfy

$$n_h m_h v_h + n_e m_e v_e + v_i \left(n_i m_i + \sum_{j=1}^{imp} n_j m_j \right) = 0 \qquad (3)$$

Here, n,m and v respectively refer to species density, mass and velocity parallel to the magnetic field. The subscripts h, i, j and e respectively relate to the heated minority species, majority ions, impurity ions and electrons. As mentioned above, in the present case, v_e is produced by the dragging of electrons by the heated minority and background ions and therefore v_e can attain a value such that $v_e \le v_h$. Thus the electron term in Eq. (3) can be neglected ($n_h \ne 0$) when

$$\frac{n_e m_e}{n_h m_h} \ll 1 \qquad (4)$$

Eq. (3) also indicates that the minority and the background ions drift in the opposite directions. The electron collision frequency with an ionic species varies as $n_{ion} Z_{ion}^2$. Consequently, in the steady state, the electron parallel drift speed v_e must obey the following equation [6]:

$$n_h Z_h^2 (v_h - v_e) + (v_i - v_e) \left(n_i Z_i^2 + \sum_{j=1}^{imp} n_j Z_j^2 \right) = 0 \qquad (5)$$

6

The total driven current including the effect of background species can be written as

$$J_T = e \left[n_h Z_h v_h + \left(n_i Z_i + \sum_{j=1}^{imp} n_j Z_j \right) v_i - n_e^* v_e \right]$$ (6)

where n_e^* refers to the density of passing (or untrapped) fraction of electrons that take part in the current carrying process. Substituting the values of v_e and v_i in terms of v_h from Eqs (3 and 5) and using the quasi-neutrality property of the plasma,

$$n_e = n_h Z_h + n_i Z_i + \sum_{j=1}^{imp} n_j Z_j$$ (7)

and defining the effective charge of the plasma Z_{eff} as

$$Z_{eff} = \frac{1}{n_e} \left[n_h Z_h^2 + n_i Z_i^2 + \sum_{j=1}^{imp} n_j Z_j^2 \right],$$ (8)

the total driven current J_T can be written in the following form:

$$J_T = J_h \left[1 - \frac{Z_h}{Z_{eff}} - \left\{ \frac{\lambda m_h [Z_i n_i (1 - \frac{Z_i}{Z_{eff}}) + \sum_{j=1}^{imp} Z_j n_j (1 - \frac{Z_j}{Z_{eff}})]}{Z_h (n_i m_i + \sum_{j=1}^{imp} n_j m_j)} \right\} + \right.$$

$$\left. (1 - \frac{n_e^*}{n_e}) \left\{ \frac{Z_h}{Z_{eff}} - \frac{\lambda m_h \left(n_i Z_i^2 + \sum_{j=1}^{imp} n_j Z_j^2 \right)}{Z_h Z_{eff} \left(n_i m_i + \sum_{j=1}^{imp} n_j m_j \right)} \right\} \right]$$ (9)

where J_h represents the (heated species) minority ion current for which an expression in the normalized form is given below in Eq. (13). Here, λ is a parameter that depends on the toroidal background ion rotation v_i. In this paper, we take it to be unity. A situation in which $0 \le \lambda < 1$, can be produced by injecting a low-energy beam of majority particles [11]. Since MCD increases by reducing λ, an appropriate amount of rotation by neutral beam injection could improve MCD efficiency (see also Section 6). The factor $(1-n_e^*/n_e)$ in Eq. (9) represents the trapped electron fraction which can be written as [18]

7

$$1 - \frac{n_e^*}{n_e} \simeq 1.46\sqrt{\varepsilon}\, A(Z_i) \tag{10}$$

where $A(Z_i)$ is tabulated in [18]. For example, $A(Z_i) \cong 1.68$ for $Z_i = 1$. Here, ε is the inverse aspect ratio (r/R_0) and R_0 is the major radius of the tokamak. For an easy physical interpretation, we rewrite Eq (9) in the limit of $n_j = 0$ $(j = 1,...\text{imp})$:

$$J_T = J_h\left[1 - \frac{Z_h}{Z_{eff}} - \frac{\lambda m_h Z_i}{m_i Z_h}(1 - \frac{Z_i}{Z_{eff}}) + (1.46\sqrt{\varepsilon}\, A(Z_i))\left\{ \frac{Z_i}{Z_{eff}}(\frac{Z_h}{Z_i} - \frac{\lambda m_h Z_i}{m_i Z_h}) \right\} \right] \tag{11}$$

In Eq. (11) unity (in the 1st term) clearly represents the minority ion current for which an expression is given below in Eq. (13). The 2nd term with a negative sign is due to the dragging of electrons by the fast ions and the magnitude of the contribution relates to the situation as if there were no trapped electrons. The 3rd term contains two contributions: (i) the unity represents the background ion return current due to their rotation opposite to the minority ions and (ii) dragging of elctrons by background ions (again as if there were no trapped electrons) which decreases the background ion return current. Finally, the last term now represents the effect of trapped electrons and again contains two contributions: (i) due to fast ions (increases J_T) and (ii) background ions (decreases J_T). The contribution of the last term varies as $\sqrt{\varepsilon}$ and reduces to zero as we approach the axis.

Equation (11) is further simplified in the limit of small minority ion concentration $(Z_h^2/Z_i^2)/(n_h/n_i) \ll 1$ such that $Z_{eff} = Z_i$ leading to the expression given in Ref. 11,

$$J_T = J_h\left[1 - \frac{Z_h}{Z_{eff}} + \left(1.46\sqrt{\varepsilon}\, A(Z_i)\right)\left\{ \frac{Z_h}{Z_{eff}} - \frac{\lambda m_h Z_i}{m_i Z_h} \right\} \right] \tag{12}$$

In the above, an expression of J_h remains to be found. We do not present the details of the derivation of J_h which are given by Fisch [6]. However, to be consistent with our previous treatment, we take the presence of additional impurity ion species into account and obtain the normalised current drive efficiency in a notation similar to that of Fisch [6] as follows:

$$\left(\frac{J_h}{P_d} \right)_n = \frac{3}{Z_h \Delta}\left(\frac{u\, w}{(1 + Yu^3)^2} \right) \tag{13}$$

where

$$Y = \frac{1}{3}\left(\frac{2}{\pi} \right)^{1/2}\left(\frac{m_e}{m_h} \right)^{1/2}\frac{1}{\Delta}, \tag{14}$$

and

8

$$\Delta = \frac{n_i Z_i^2}{n_e} \left(1 + \frac{m_h}{m_i}\right) + \sum_{j=1}^{imp} \frac{n_j Z_j^2}{n_e} \left(1 + \frac{m_h}{m_j}\right) \tag{15}$$

and

$$w = \frac{v_{//}}{V_N} = \frac{(\omega - \omega_{ch})}{k_{//} V_N} \tag{16}$$

and $u = v/V_N$, $V_N = \sqrt{(T_e/M_h)}$. See below for normalization factors of J_h and P_d. Note the above definition of V_N which was not explicitly defined in Ref. 6. Here, ω_{ch} is the minority ion cyclotron frequency and $k_{//}$ is the wave propagation constant parallel to the magnetic field determined by the spectrum excited by the phased antenna array. Note the appearance of impurity ion terms in the factor Δ which were neglected in Ref. 6. Also, the background ion charge appears explicitly in our formulation which was specialized to unity in Ref. 6.

In the above, v is the minority ion velocity obtained from Stix calculation [10] for a given ICRH power density P_d on a flux surface. The Stix calculation is slightly modified as follows to suit the purposes of minority current drive calculation. The normalized minority velocity u is determined by

$$u = \frac{v}{V_N} = \frac{2 < E >}{T_e} \tag{17}$$

where $< E >$ is the average energy of the minority ion distribution function [10] from which the minority background Maxwellian distribution has been subtracted out. This reflects the velocity v of the heated species obtained from $< E >$ more correctly as otherwise the average energy calculation is dominated by the background Maxwellian part rather than the heated tail.

In Eq. (13) we have normalized J_h by $e n_e v_{te}$ and P_d has been normalized by $\nu_0 n_e m_e v_{te}^2$ where the electron thermal velocity is defined as $v_{te} = \sqrt{(T_e/m_e)}$ and ν_0 can be obtained from [19] as

$$\nu_0 = \frac{4\pi \ln \Lambda n_e e^4}{v_{te}^3 m_e^2} \tag{18}$$

We also note that in the limit of $n_j = 0$ (j = 1,...imp) and $Z_i = 1$ with $n_h Z_h^2/n_i \ll 1$ and neglecting the effects of electron trapping, Eq. (11) reduces to Eq. (27) of Ref. 6 where

$$\eta \equiv \left(\frac{J_T}{P_d}\right)_n = \left(\frac{J_h}{P_d}\right)_n (1 - Z_h) \tag{19}$$

9

where the sign of the term $(1 - Z_h)$ is inversed due to difference in normalization of J_h by $-en_e v_{te}$ in Ref. 6.

Finally, in practical units, we can write the driven current per unit power as follows:

$$\frac{I(A)}{P(W)} = 0.061 \left(\frac{T_e(keV)}{R_0(m)n_e(10^{20}m^{-3}) \ln \Lambda} \right) \cdot \eta \tag{20}$$

where R_0 is the major radius and $\ln \Lambda$ is the Coulomb logrithm and η now includes the full expression of J_T given in Eq. (9) rather than the simplified expression (19) used in Ref. 6.

The expression (16) of w which appears in Eq. (13) of the current drive efficiency suggests that the sign of the driven current changes on the two sides of the minority cyclotron layer. If the wave is only partially absorbed before it crosses the layer, the net driven current may be small but it can change the gradient of the current density locally. This has been exploited to control the sawtooth period in JET when the cyclotron layer is located at $q = 1$ surface on the high field side (see section 3). Also, note that the width of the two lobes of current drive around the minority cyclotron layer is governed by the cyclotron Doppler broadening i.e. the $k_{//}$-spectrum and the minority ion temperature. The former depends on the phasing of the antenna array.

In the analysis presented above, the effect of minority ion trapping has not yet been included which appears more naturally in the alternative approach of solving the Fokker-Planck equation in the toroidal geometry. As mentioned above, the minority current drive efficiency is optimum when the minority energy $E \approx E_c$. In such a regime, the minority energy distribution function can be assumed to be isotropic due to the effect of pitch angle scattering. In this case, the effect of minority ion trapping can be included in a simple way by reducing the number of passing minority ions that take part in the current carrying process by a factor

$$f_T = 1 - \sqrt{\varepsilon(1 + \cos \theta_p)} \tag{21}$$

where θ_p is the poloidal angle in the toroidal geometry used in the ray tracing and $\varepsilon \leq 0.5$. This effect is taken into account at each step of the ray in the plasma cross section. As mentioned before, this effect does not take care of the Ohkawa effect and is not included in our treatment.

2.5 Sawtooth Stabilization Mechanisms. Experiments in JET have shown that sawteeth can be stabilized by ICRH in two ways: (i) Due to fast ion production when the antenna straps are phased such that $\Delta\phi = 0$ or π and the minority ion cyclotron layer is located near the plasma centre. But, if the cyclotron layer is located off-axis (radius roughly greater than the $q = 1$ surface), sawtooth stabilization does not occur.

(ii) If the cyclotron layer is located close to the $q = 1$ surface, and $\Delta\phi \neq 0, \pi$, the sawteeth can again be stabilized by a reduction of the local shear (dq/dr) at the $q = 1$ surface. Assuming that sawtooth relaxations are triggered by resistive internal kink modes [20], the stability analysis given elsewhere [7,21] suggests a 'practical' criterion for stability as follows:

$$-\hat{\lambda}_H \equiv \frac{[\delta W_{MHD} + \delta W_{hot}]}{\varepsilon_\eta^{1/3}} > O(1) \tag{22}$$

where the right hand side is a quantity of order unity and its exact value depends mainly on the normalized diamagnetic frequency $\hat{\omega}^* \equiv \omega^* i/\omega_A$. Here, δW_{MHD} is the ideal MHD energy functional for internal kink perturbations and δW_{hot} is the fast particle perturbed energy and $\varepsilon_\eta \equiv \eta c^2 s_1^2/(4\pi r_1 \omega_A^2)$ is the inverse magnetic Reynolds number. Also, η is the resistivity, r_1 refers to the radius of $q = 1$ surface, s_1 is the magnetic shear (rdq/dr) at the $q = 1$ surface, $\omega^* i = - (c/Z_i e B_r n_i)_1 (dp/dr)_1$ where the subscript 1 indicates that the values are to be evaluated at the $q = 1$ surface. Further, $\omega_A = V_A/R$ where V_A is the Alfven velocity and R is the major radial location. Since this paper is primarily concerned with the sawteeth control by the modification of shear at the $q = 1$ surface which requires ICRH power deposited off-axis (near $q = 1$), therefore, we neglect the effects of hot particle perturbed energy that are effective in stabilization when the heating is on-axis and the fast-ion pressure profile is well peaked within the $q = 1$ surface. If the β_p (ratio of kinetic pressure to poloidal magntic pressure) within the $q = 1$ surface is smaller than the ideal MHD threshold value for β_p, then δW_{MHD} is positive and

$$\frac{\delta W_{MHD}}{\varepsilon_\eta^{1/3}} \propto s_1^{-5/3} \tag{23}$$

where s_1 represents the shear at the $q = 1$ surface. This means that the stability criterion can be more easily satisfied by reducing the shear at the $q = 1$ surface. A stabilization of the sawtooth is achieved by the minority dipolar current driven across the $q = 1$ surface in such a way so as to reduce the current inside and increase the current outside the $q = 1$ surface therby reducing (flatten) the shear at the $q = 1$ surface. A destabilization (reduction in sawtooth period) can be achieved by a similar dipolar current but with their directions inversed. In practice, for a given configuration of minority current drive, this is achieved simply by reversing the phase difference ($\Delta\phi$) between straps of the ICRH antenna, for example, from $+ 90°$ to $- 90°$.

In section 3, we present the experimental results of stabilization and destabilization of sawteeth by such a phase reversal and the resulting sawtooth period will be compared with theoretical estimates in the following way. For the given plasma and antenna parameters and the phased ICRH power applied in the experiment, we determine the dipolar current driven under the minority scheme including the effect

of the TTMP electron current drive as calculated by the procedure outlined above. The effect of this driven current on the stability of resistive internal kink modes is then assessed by a numerical code that involves (i) an equilibrium code [22], (ii) a transport code [23] that monitors the time evolution of the total current density (ohmic + RF), (iii) experimental profiles of temperature and density and (iv) a code [24] to evaluate ($\delta W = \delta W_{MHD} + \delta W_{hot}$) based on an aspect ratio expansion [25]. The aim is to compute the stability parameter

$$\hat{\lambda}_H \equiv - \frac{\delta W_{MHD}}{\varepsilon_\eta^{1/3}} \qquad (24)$$

as a function of time during a sawtooth ramp starting at the bottom of the ramp. The period of the stabilized sawtooth due to minority current in this simulation is defined as the time it takes for $\hat{\lambda}_H$ to evolve from a large negative values (stable region) to that of a threshold value $- \hat{\lambda}_H = O(1)$ where it moves into unstable region and the sawtooth crash occurs. This threshold value is model dependent and involves considerations such as diamagnetic effects, ion Larmor radius, electron inertia, electron thermal conductivity and neo-classical effects. But, for the JET discharges presented here, most models converge to give a threshold value of order unity as mentioned above. The simulation results are presented in a form in which time trajectories are drawn in the ($\hat{\omega}*, \hat{\lambda}_H$)-plane. The simulated sawtooth period corresponds to the time the trajectory takes to cross the stability boundary starting from an initial point in the ($\hat{\omega}*, \hat{\lambda}_H$)-plane corresponding to the bottom of the sawtooth ramp where relaxed q, T_e, and n_e-profiles are assumed [26]. Sensitivity studies have been performed to verify that the simulated sawtooth period does not depend strongly on the details of the initial profiles [26].

3. EXPERIMENTAL RESULTS.

In this section we present the experimental data on the sawtooth stabilization and destabilization under the minority current drive scheme where the local shear at the q = 1 surface is modified by locating the cyclotron layer close to the q = 1 surface. The sawtooth period variation as a function of ICRH power which has an optimum level is also analysed. Further, we present data analysis of the sensitivity of the sawtooth period on the closeness of the minority cyclotron layer and the q = 1 surface in toroidal field ramp-up or ramp-down experiments both for sawtooth stabilization and destabilization schemes. A comparison of experimental results of sawtooth period with the theoretical predictions using the model described in Section 2 are given in Section 4.

3.1 Configuration for Current-Drive Experiments.
JET (Joint European Torus) is a D-shaped large tokamak [27] with major radius $R_0 = 2.96$ m, minor radius $a_p = 1.2$

m, nominal toroidal field $B_\phi = 3.4$ T, plasma current $I_p \leq 7$ MA, and plasma elongation $= 1.6$. For the results presented in this paper, $I_P = 2$ MA, the toroidal field was varied between $2.4 < B_\phi < 3.4$ and the ICRH frequency of operation $f = 42.7$ MHz was used. The plasma composition was a mixture of hydrogen and deuterium gases with $0.1 < n_H/n_D < 0.3$. The ICRH system of JET [28,29] consists of a total generator power of 32 MW, 20 s, 23-57 MHz and uses eight antennas that were distributed symmetrically around the torus. The current drive experiments presented here were carried out using JET A1-antennas which have now been replaced with A2-antennas for the new divertor phase of JET. A JET A1-antenna had two radiating elements that were separated toroidally. In the present experiments, they were energized at moderate power levels typically at a total power of 5 MW except for power scaling experiments where it ranged from $1.2 < P_{RF} < 14MW$. The antenna straps were driven [30] with a phase difference $\Delta\phi = +90°$ or $-90°$ depending on the scenario of stabilization or destabilization and whether the cyclotron layer was located on the high-field or low-field side. The antenna screens are made of one tier of beryllium rods [31]. We note that ICRH specific impurities have been reduced to negligible levels in all conditions of ICRH operation in JET.

For general tokamak diagnostic systems including that of JET see, for example, a review paper by Orlinskij and Magyar [32] and references therein. In the results presented here, sawteeth period was principally determined from the electron temperature (T_e) data obtained by the soft X-ray technique [33]. The inversion radius ($R_{inv} \cong R_{q=1}$) was estimated from the soft X-ray, electron cyclotron emission (ECE) and Faraday rotation polarimeter diagnostics [34].

As mentioned in the introduction, sawtooth stabilization or destabilization occurs when the local shear at the $q = 1$ surface is decreased or increased respectively. In the minority current drive scheme, where the current reverses its sign on the two sides of the cyclotron layer, the above modification in shear can be accomplished in several ways. For a better undersatnding, we show in Fig. 2, a schematic view of JET from top in which the layout of 2-straps of an antennna, the direction of I_P, B_ϕ and the fast-wave propagation for a given $\Delta\phi$ is indicated. Also we draw schematically an ohmic current density (J) profile together with locations of two cyclotron layers (near the $q = 1$ surface) one at low-field side (LFS) and the other at high-field side (HFS) of the tokamak. The driven minority ion current for a phasing of $\Delta\phi = +90°$ is as shown by arrows on the two sides of the cyclotron layer. In such a configuration, if the minority cyclotron layer (R_{CH}) is located on the HFS, the flow of minority current is such as to flatten the J-profile or decrease the shear (stabilization), whereas if R_{CH} is located on the LFS, the J-profile becomes steeper and the shear increases (destabilization). However, the fast-wave interacts simultaneously with electrons via e-TTMP and e-LD and drives a current in the direction shown by the e-TTMP arrow. In this phasing, note that the electron current opposes the inner lobe of ion current on the HFS and aids the one at LFS. In scenarios where shear reversal is beneficial

(see Section 5) for confinement improvement, the R_{CH} can be moved towards the centre to take full advantage of the two drives simultaneously. In the case, when $\Delta\phi = -90°$, the ion current drive at the HFS and LFS together with the electron current is inversed. Thus 4 different configurations can be operated as shown in Table 1. Note that minority ion trapping effects are higher when R_{CH} is located on the LFS.

3.2 Sawtooth Stabilization and Destabilization. As mentioned in the last section, the shear at the q = 1 surface can be modified by locating the R_{CH} at the HFS or the LFS. But, in this section, we present the results of stabilization and destabilization only in the HFS case. Some evidence of LFS destabilization is presented in the next section in the B_ϕ ramp-up experiments. The minority current drive effects on the LFS are reduced due to the increased trapping of minority ions and due to Ohkawa effect mentioned above.

In Fig. 3, the measured soft X-ray intensity is plotted as a function of time for two shots under minority current drive scheme when the R_{CH} is located close to the q = 1 surface on the HFS. These experiments were carried out in a D-plasma with hydrogen as minority species. The plasma parameters are given in Table 2, case: JET-A1. Three of the 8-antennas were energized and the total RF power was about 4-5 MW. To present the evidence more succinctly but clearly, in shot 24896, we drove the two straps of an antenna initially in the heating phase with a $\Delta\phi = 180°$ (dipole) and then switched to a value of $\Delta\phi = +90°$(current drive phasing). Note that when $\Delta\phi = 0$ or π, the excited antenna $k_{//}$-spectrum is symmetric and no current is driven. During the dipole phase, the ohmic sawteeth are only mildly affected by the ICRH power as the cyclotron layer is located off-axis at the q = 1 surface. However, during the time when $\Delta\phi = +90°$, sawtooth stabilization occurs. The stabilized sawtooth crashes after a certain time either due to the expansion of the q = 1 surface (R_{CH} is fixed) or the β_{p1} (poloidal beta within the q = 1 surface) exceeds the ideal MHD threshold value of the β_p [7].

All other conditions maintained as in shot 24896, we simply change, in shot 24898, the phase between the antenna straps from 180° to 0 in the heating phase and +90° to −90° in the current drive phase. There is little change in the sawteeth period in the heating phase but, the sawtooth behaviour is dramatically changed during the current drive phase. The soft X-ray intensity or the relative T_e is lower and the sawteeth are smaller and more frequent as can be seen more clearly in the inset in which a part of the trace has been expanded. A change of phase from +90 ° to -90 ° results in a change in the sawtooth period from 640 ms to 32 ms. In the destabilized case, the ECE T_e-profile (not presented) shows that it is quite flat up to the inversion radius as compared to the stabilized case where it was peaked despite the off-axis heating. Note that the power trace is somewhat ragged in the CD phase as in this case the automatic feedback control was switched from power to the antenna current (phase and amplitude) therefore, the power coupled to the plasma was dependent on the

14

coupling resistance and the circulating power between the two straps. The effect of circulating power can be taken care of by using a conjugate box [30] that was not used in these first experiments of current drive in JET.

3.3 Sawtooth Period Dependence on RF Power. As mentioned in the introduction, the minority ion current drive is maximum when the minority ions interact equally with electrons and background (see section 4.1.1) which occurs when the minority ion average tail energy is close to the critical energy E_c (see Eq. 2). According to Stix [10], the parametric dependence of the tail temperature can be written as

$$T_{tail} \sim \frac{m_h}{Z_h^2} \cdot \frac{1}{n_h} \cdot \frac{<P>}{n_e} \cdot T_e^{3/2} \tag{25}$$

where $< P >$ is the flux surface averaged power density in the minority species. From Eq. (25), it is clear that for a given minority species, its concentration and electron temperature, the tail energy increases with increasing $< P > /n_e$. For an (H)-D plasma $E_c \approx 10T_e$ (see Table 3), it is thus possible to increase the tail energy by increasing the RF power (P_{RF}) and overshoot the optimum value for obtaining the longest sawtooth period. Such a behaviour is shown in Fig. 4 where ECE measured T_{e0} time traces are shown for several power levels with a $\Delta\phi = + 90°$ and the R_{CH} was located near the q = 1 surface on the HFS. From the inset, where the longest sawtooth period has been plotted as a function of P_{RF}, we note that for the parameters used in this experiment, the maximum sawtooth period (τ_{smax}) is obtained with a modest power level of 3-5 MW and beyond this level τ_s decreases with increasing P_{RF}. Repeating the same experiment at higher minority concentration [3], it was found that τ_{smax} occured at higher power level. Further, at a fixed power level but now increasing the minority concentration, an optimum concentration was found [3] for τ_{smax}. The dependence of T_{tail} on other parameters (Eq. 25) allows us to predict the τ_{smax} behaviour for current drive scenarios with other minority species such as He3, D etc. (see also section 4.1.1).

3.4 Sensitivity of $| R_{CH} - R_{q=1} |$ on Sawtooth Control. As mentioned above, the sawtooth instability can be controlled by modifying the magnetic shear at the q = 1 surface. This is accomplished by MCD in which the R_{CH} layer is placed close to the q = 1 surface. In this section, we investigate the sensitivity of relative positioning of the R_{CH} with respect to the $R_{q=1}$ on the sawtooth period both for stabilization and destabilization. However, the results presented are influenced by the fact that the $R_{q=1}$ itself expands as the sawtooth is stabilised (see below). Also, we need to determine both R_{CH} and $R_{q=1}$ as accurately as possible.

In the calculation of the cyclotron layer position, we take account of the paramagnetic (poloidal field) and diamagnetic (β_p) effects of the plasma, albeit approximately, on the total magnetic field [35]. A better evaluation can be done by the plasma equilibrium identification codes such as IDENTC [22] used at JET. The values used here are within 0.8% [36], when compared to those calculated from IDENTC. For

the data of shots presented ($I_P = 2MA$), the values of R_{CH} are typically 4-5 cm higher than those calculated from the vacuum magnetic field alone [36]. The q = 1 surface is assumed to be close to the sawtooth inversion radius. The latter can be determined by three different diagnostics: (i) an analysis of the T_e profile from ECE measurements just before and just after a sawtooth crash. (ii) soft X-ray tomographic reconstruction and (iii) Faraday polarimetric measurements giving a q-profile at desired time slices. Note that (i) and (ii) give q = 1 location only at sawtooth crashes. In Fig. 5, we show a comparison of the $R_{q=1}$ and its evolution during a monster sawtooth [37] (ICRF heating on axis) and stabilization resulting from the fast ion pressure (δW_{hot}) [24] (see Eq. 22). The three different diagnostics show that the q = 1 surface radius expands during a monster sawtooth but a quantitative agreement between the three methods is good only at the begining of the sawtooth and it becomes poorer as time evolves. A critical discussion of the error-bars involved in the three methods is beyond the scope of this paper. But, in the present analysis, we use R_{CH} obtained from the soft X-ray tomographic reconstruction carried out from the data taken by about 200 diodes.

3.4.1 Sawtooth Stabilisation.

In Fig. 6, we present the time traces of the soft X-ray intensity (I_{SXR}), DD-reaction rate (R_{DD}), ICRH power applied (P_{RF}) in a shot in which toroidal filed (B_{TOR}) was ramped up to vary the R_{CH} position as a function of time. The phase difference between the two antenna straps was $\Delta\phi = +90°$ (for stabilization) and the R_{CH} crosses the $R_{q=1}$ surface on HFS (inboard). But, in terms of the radius in poloidal cross section, r_{CH} was decreasing when crossing the $r_{q=1}$ surface. The τ_{st} deduced from the soft X-ray signal is also plotted (see the last trace) and ascribed to the begining of the sawtooth. We note that τ_{st} is maximum when R_{CH} is close to $R_{q=1}$ as expected. The origin of a longer sawtooth at t = 7.5s is not clear. Note that R_{DD} ramps up during the stabilised sawtooth period and was found to be a characteristic of all sawtooth stabilised by minority current drive.

In Fig. 7, we present another shot with the same signals as in Fig. 6 in which the B_{TOR} was ramped down. Again, the R_{CH} crosses the $R_{q=1}$ surface on the HFS but now the r_{CH} is increasing as compared to the previous case of Fig. 6. In this case the behaviour of the τ_{st} is markedly different and has a broad maximum at $R_{CH} = R_{q=1}$. First, we point out that the ramp rate of R_{CH} is different in the two cases: +6.5 cm/s for B_{TOR} ramp-up and -4.5 cm/s for B_{TOR} ramp-down which could partially account for the difference in the two cases. However, we also note that in the ramp-down case, both the q = 1 surface and the r_{CH} increase simultaneously whereas in the previos case one was increasing and the other was decreasing. In Fig. 8, we plot the τ_{st} as a function of the difference between R_{CH} and $R_{q=1}$ for the ramp-up and ramp-down cases. The τ_{st} decreases by a factor of 2 when $| R_{CH} - R_{q=1} |$ is approximately 6 and 12 cm in the B_{TOR} ramp-up and ramp-down cases respectively.

16

3.4.2 *Sawtooth Destabilisation.* In Fig. 9, we present time traces of same signals as those in Fig. 6 with B_{TOR} ramp up. The R_{CH} located on HFS thus varied around the $R_{q=1}$ surface. Since in this case $\Delta\phi = -90°$, destabilisation of sawteeth is expected. The τ_{st} as shown does indeed has a minimum when R_{CH} crosses the $R_{q=1}$ surface. We show the results of another shot in Fig. 10 in which the R_{CH} was varied around the $R_{q=1}$ surface but this time on the LFS (outboard). In this case, $\Delta\phi = +90°$ was used for destabilization. Indeed, sawteeth become very tiny and their period decreases sharply when $R_{CH} = R_{q=1}$. On the LFS, the effect of minority ion trapping is stronger. In the very few experiments done on the LFS, sawtooth stabilisation on this side was not seen clearly.

4. COMPUTED RESULTS AND A COMPARISON WITH EXPERIMENT.

In this section, we present results computed from codes based on the models outlined in Section 2. First, we present normalised minority current drive efficiencies for different scenarios in which the minority and majority ion combination is changed. We then discuss the theoretical results of the modification of current density (J) profile, safety factor (q) profile and the magnetic shear (r/q dq/dr) profile in the MCD scenarios with a view to controlling the sawtooth instability (stabilization and destabilization). Finally, as an illustration, we will also present the results of the stability analysis of the resistive internal kinks for the shot 24896 presented in Section 3. In the simulation, the shear profile is modified by the minority current drive calculated above. We compare the predicted sawtooth period from theory to that observed experimentally. This represents a full simulation of sawtooth period from our codes (see Fig. 1) for a representative shot using experimental data of the antenna and plasma parameters, profiles, input power, minority ion concentration, phasing and directivity.

4.1 Normalized Current Drive Efficiencies. In this subsection, first we compare the normalized heated minority CD efficiencies (see Eq. 13) and the net (including background species response) normalized CD efficiency (see Eq. 9) for several scenarios. Then we illustrate the effect of electron trapping, ion trapping, background ion rotation and impurity species on the net CD efficiencies.

4.1.1 *Effect of Charge and Mass of Minority and Majority Ions.* To discuss which (minority)-majority ion combination have the highest MCD efficiency, we first note from Eq. 13 that for a fixed value of w and a given mixture of plasma species, the highest efficiency occurs at $u = (5Y)^{-1/3}$. The maximum value of MCD efficiency is then

$$\eta^{max} = \frac{3w}{Z_h\Delta} \frac{25}{36} (5Y)^{-1/3} \qquad (26)$$

17

Neglecting the impurity species and assuming $n_h/n_i \ll 1$, we find that

$$\eta^{max} \sim \eta(Z,m) \frac{V_\parallel}{\sqrt{T_e}} \tag{27}$$

where the efficiency dependent on Z and m of minority and majority species is given by

$$\eta(Z,m) = \frac{1}{Z_h} \left(\frac{m_i m_h}{Z_i(m_i + m_h)} \right)^{2/3} \tag{28}$$

Here, h refers to the minority and i to the majority ion species. The value of $\eta(Z,m)$ is tabulated in Table 3 for several majority and minority scenarios. We find that (D)-T has the highest relative value and (H)-He3 the smallest. However, note that these values do not yet include the background plasma response (see below). Normalised minority CD efficiencies (see Eq. 13 which includes impurity species and arbitrary value of n_H/n_e) are now plotted as a function of minority ion average energy $<E>$ in Fig. 11 for (H)-D, (H)-He3, (D)-T and (He3)-D scenarios. The parameters used for this comparison are given in Table 2, case: JET-A1 with $f - f_{CH} = 1.8$MHz. Note that the efficiency for each scenario peaks when the $<E>$ is near the critical energy E_c (see Table 3) at which the minority ion relaxes roughly equally both on bakground electrons and ions. This was noted by Fisch [6] as the condition for maximum minority CD since the relative drift between minority and majority ions depends on the variation of the collision frequency v with speed of the minority ion which is strongest at $E = E_c$. For $E \ll E_c$ minority ions collide heavily with majority and for $E \gg E_c$ they collide principally with electrons resulting in lower Vv (with speed) and lower efficiency.

Now we take the response of the background species including the effect of electron and ion trapping in to account (Eq. 9). In Fig. 12, we plot the net MCD efficiency as a function of $<E>$mino for the four scenarios mentioned above. We have taken $\varepsilon = 0.15$ on the HFS and $\lambda = 1$ is assumed. We find that the efficiencies are much reduced especially for the (He3)-D scenario. The net MCD efficiency is reduced since a part of the plasma response drives current in the opposite direction. In Fig. 13, we plot the MCD constituent factors as a function of $<E>$mino for (H)-D scenario in which J_M, J_{cB}, J_{cM} and J_{iB} refer respectively to the minority current, background ion dragged electron current, minority ion dragged electron current and background ion current as discussed just after Eq. (11). Note that J_{cM} and J_{iB} are of a sign opposite to the minority ion current and thus reduce the net current drive.

4.1.2 *Effect of Electron Trapping.* The electron trapped fraction is given by Eq. 10. For example, at the magnetic axis ($\varepsilon = 0$), the trapping is zero and the minority dragged electrons cancel the minority current completely in a (H)-D plasma if there are no impurity species ($Z_{eff} = 1$). In the toroidal geometry, the electron trapping off

18

axis has a beneficial effect on the minority current drive. For an (H)-D and a (He3)-D plasma with $n_c = 0.025$, we plot in Fig. 14, the net current drive efficiency for $\varepsilon = 0$ and 0.15 (HFS). We find that for (H)-D plasma, the efficiency is reduced when $\varepsilon = 0$ but in the case of (He3)-D plasma the efficiency even becomes negative since $|J_{eM}|$ is larger than the $|J_M|$ due to $Z_h > Z_{eff}$ (see Eq. 12). That is why (He3)-D scenario has the least efficiency in Fig. 12.

4.1.3 *Effect of Ion Trapping.* In the energy range where the MCD efficiency is highest, the minority ion distribution function can be assumed to be isotropic. In such a case, the minority ion trapped fraction is given by Eq. (21). For an (H)-D plasma, in Fig. 15 we plot the net MCD efficiency as a function of $<E>$ mino for $\varepsilon = 0.15$ inboard and outboard locations in the mid plane. The efficiency is reduced by more than a factor of 2. This shows why the stabilization or destabilization of sawtooth is easier on the inboard location (see Section 3). We note that in our calculations the Ohkawa effect is not taken into account which may reduce the efficiency even further due to ion trapping.

4.1.4 *Effect of Background Ion Rotation.* In Fig. 16, we plot the net MCD efficiency as a function of $<E>$ mino for two values of the parameter λ in an (H)-D plasma. We note that the efficiency reduces roughly by a factor of 2 due to the background ion rotation. For the modeling presented in this paper, we use $\lambda = 1$ throughout.

4.1.5 *Effect of Impurity Species.* Finally, we present the effect of carbon impurity species or Z_{eff} on the MCD efficiency in Fig. 17 where two curves are compared one with $n_c/n_e = 0$ and the other with 0.025. We note that the net MCD efficiency is reduced by increasing the impurity concentration. A significant reduction occurs in the MCD efficiency itself due to increased collisions with background ion species. Note that there is little change in MCD efficiency at higher energies where the minority collides predominantly with electrons and the addition of a small concentration of impurity ion is of little significance.

4.2 Minority Current Density and Shear Profiles. Using the ensemble of codes presented in Section 2 (see Fig. 1), we now present the results of our model of e-TTMP and minority current drive for the parameters (see Table 2, case: JET-A1) corresponding to those of the JET experimental shots 24896 and 24898 made in (H)-D plasmas (see Fig. 3).

4.2.1 *Sawtooth Stabilization Phasing.* In shot 24896, the minority cyclotron layer R_{CH} was located near the $q = 1$ surface on the HFS and the phase difference between the two straps of energized antennas is $\Delta\phi = +90°$. The directivity of the $k_{\parallel}$-spectrum excited is $D \cong 0.6$. In Fig 18 (a), we show the current density profile (J) that are obtained by applying a 4.5 MW of RF power at 42.7 MHz to a JET plasma. The excited fast wave with asymmetric $k_{\parallel}$-spectrum interacts both with electrons and ions

and drives noninductive current. The e-TTMP CD peaks at the centre whereas the minority CD changes sign at the cyclotron layer position. In accordance with Table 1 and Fig. 2, the e-TTMP current in this case adds to the ohmic current and the signs of the two lobes of the minority current are as shown. We also show the initial ohmic current density profile as well as the total J-profile (OH + e-TTMP + MCD). In the latter, the ohmic current (inductive) contribution was reduced so as to maintain the total plasma current at 2 MA. We note that due to the dipolar nature of the MCD profile, the J-profile at the $q = 1$ surface in this case has been flattened as compared to the ohmic case. This leads to sawtooth stabilization. The corresponding tokamak magnetic shear profiles are shown in Fig. 18(b) which shows that the shear decreases at the $q = 1$ surface. The J-profiles presented here will be used as input to the internal kink stability code in Section 4.2.3 where we compare the sawtooth period in the ohmic and current drive phases of the discharge.

4.2.2 *Sawtooth Destabilization Phasing.* In shot 24898, all the conditions were the same as in shot 24896 except the phase difference between the two straps of excited antennas is changed to $\Delta\phi = -90°$. In Fig 19 (a) and (b), we show the current density profile and the shear profiles both for the ohmic as well as the CD case. Again, in accordance with Table 1 and Fig. 2, the e-TTMP current in this case opposes the ohmic current and the signs of the two lobes of the driven minority current are also reversed as shown. We note that in this case, the current density profile is steepened and the shear increases at the $q = 1$ surface. This leads to sawtooth destabilization as shown in Fig. 3. In this phasing, the reversed e-TTMP CD direction makes the additional effect of shear reversal within the $q = 1$ surface. However, the total combined shear reversal is small as the minority CD inner lobe and TTMP CD oppose each other. An increased shear reversal scenario for high energy confinement regimes will be presented in Section 5.

4.2.3 *Internal Kink Stability Analysis.* We now present results of the internal kink stability analysis carried out by the procedure outlined in Section 2.5. Using the calculated non inductive current drive profiles presented in Section 4.2.1 for the shot 24896 (stabilized sawteeth), we present simulation results in a form in which time trajectories are drawn in a $(\hat{\omega}^*, \hat{\lambda}_h)$-plane as shown in Fig. 20. The stable and unstable boundaries of a sawtooth of tokamak discharges are drawn (broken lines) for two values of the viscosity parameter $P = 0$ and 0.3 as shown. The parameter P [26] is defined as $P = 0.3 \sqrt{T_e m_i/(T_i m_e)} \, \beta_{el}$ where β_{el} is the β of the electrons at the $q = 1$ surface. For JET discharges P is typically 0.12. The simulation is started at the bottom of the sawtooth ramp just after the crash at $t = 7.36$ s in shot 24896 (see Fig. 3). At this time the trajectory lies to the left in the stable region. We show two cases: with (e-TTMP and MCD) and without non inductive current drive. The trace without the non inductive current drive (broken line) crosses the stability boundary in about 0.19 s. Note that the time points $(t - t_0)$ are marked with reference to the starting time. When the MCD is included in the stability analysis, we find that the trajectory

now crosses the stability boundary $P = 0$ in about 0.49 s leading to the stabilized sawtooth period $\tau_s = 0.49$s. In the experiment the sawtooth crashed in 0.64 s. The agreement would be somewhat better if the stability boundary is taken to be at the viscosity parameter $P = 0.12$, a value typical of JET discharges. We also present these results in another form in which the stability parameter $\hat{\lambda}_h$ is plotted as a function of time in the inset of Fig. 20 for the above two cases: with and without MCD. In this plot, the stability boundary is drawn by a broken straight line at $\hat{\lambda}_h = -1.15$ as deduced from the main figure. The sawtooth periods are thus more explicitly presented. Simulations for the destabilzed sawteeth have also been done but are not presented here (see Ref. 26). It is found that indeed the sawtooth period is reduced but only to 70 ms whereas in the experiment it was 32 ms (see Fig. 3).

The sawtooth stability threshold presented here is dependent on several factors that were pointed out in Section 2.5. Also, the trajectory in the stability/instability depends on the q, T_e and n_e-profiles that are assumed at the starting point at the bottom of the sawtooth. The analysis presented in this section can only be expected to give the trends in the stabilization of sawteeth rather than a quantitative agreement with the experimental values. Further, the nature of the sawtooth instability is such that both in experiments and in simulations, the actual sawtooth period can be somewhat different without any apparent change in the external parameters that are under the control of an experimentalist.

5. APPLICATION TO FUTURE EXPERIMENTS.

In this section, we present fast-wave CD (e-TTMP and MCD) modeling results for the forthcoming JET experiments with a view to achieving long duration high confinement regimes by shear reversal within the $q = 1$ surface. Further, we present results as calculated from our CD model but applied for sawtooth control in next-step devices such as ITER.

5.1. Magnetic-Shear Reversal for High-Confinement Regimes. Increased shear reversal within the $q = 1$ surface similar to the high confinement pellet experiments [2], can be obtained by adjusting the location of the cyclotron layer at the desired position and by adjusting the relative magnitude and direction of e-TTMP CD and the inner lobe of the MCD. The shear reversal can be stronger if both the e-TTMP CD and the inner lobe of the MCD drive currents counter the ohmic drive. For JET configuration, it can be seen from Table 1 and Fig. 2 that such a scenario can be achieved by placing the minority cyclotron layer on the LFS and $\Delta\phi = -90°$. Such a configuration was presented in Ref. 38 where due account of minority trapping was taken but the Ohkawa effect was not included. Here, we present an alternative configuration on the HFS which is better with respect to deleterious ion trapping and Ohkawa effects. At low minority concentration, the damping is higher on HFS of the cyclotron due to

peaking of the left-handed polarization near the fast-wave cutoff. In the present calculation, by using a higher minority concentration, the damping on HFS of the cyclotron layer is diminished and that on the inner lobe is augmented to achieve the desired result. The parameters for this calculation are given in Table 2 case: JET-A2. The results of current density profiles are shown in Fig. 21 (a). The sign of the e-TTMP CD is opposite to that of the inner lobe of the MCD. Nevertheless, the safety factor q and the shear profiles given in Fig. 21 (b) and (c) respectively show that the q-profile is significantly nonmonotonic and that an important shear reversal takes place in this configuration. As it is beyond the scope of this paper, we do not present here an analysis of the stability of these profiles against MHD modes such as ballooning and infernal modes. But, we note that these profiles are of a shape similar to those that have been calculated to be stable. Furthermore, these profiles are also similar to those obtained in the JET experiments with deep pellet injection leading to pellet enhanced phase (PEP) + H-mode [2].

5.2. A Scenario of Sawtooth Control in ITER-EDA. In this section, we apply the technique of sawtooth control discussed in Section 2.5 of modifying the gradient of the current density profile at the $q = 1$ surface in ITER plasma, the parameters of which are being defined by the ongoing Engineering Design Activity (EDA). To select a suitable scenario for ITER, we plot the fundamental and harmonic cyclotron frequencies of several relevant species as a function of major radius for the ITER-EDA parameters given in Table 2. The proposed frequency range of the ITER fast-wave ICRF system is 20-85 MHz [40]. As mentioned in Section 4.1.3, from the adverse effect of ion trapping on the MCD, it is desirable to locate the the minority cyclotron layer on the HFS where trapping effects are small. But, within the constraints of frequency range of the ITER-EDA fast-wave system, only He3-minority cyclotron layer could be located at the $q = 1$ surface on the HFS in a frequency range of 65-80 MHz. However, for an antenna located outboard, operation at such a frequency encounters first the minority hydrogen and beryllium impurity cyclotron layers depositing a part of the power there. Further, before it arrives at the He3-cyclotron layer on the HFS, a significant fraction (up to 45 %) of the input power is absorbed by the e-TTMP. In addition, as we have shown in Section 4.1.1, the charge and mass of He3 is such that MCD efficiency is the worst of the four combinations. From this point of view, (D)-T scenario would have been the best but when $f = f_{CD}$ is located on the HFS, $f = 2f_{CT}$ is encountered first. Furthermore, to develop the deuterium tail significantly ($E = E_c$) at ITER-EDA high plasma densities, only 1-2% deuterium can be used which is impractical in a reactor. Therefore, we propose a LFS scenario with hydrogen as the minority ($n_H/n_e = = 0.018$) at a frequency of 74 MHz. As shown in Section 4.1.1, hydrogen minority has one of the best net MCD efficiency. Also, most of the power launched can be usefully deposited at the desired location, but depending on the minority H concentration, a little power can also go to the second harmonic heating of deuterium which in priniciple could also help to produce the dipolar ion current. We also note that in this scenario, the R_{CH}

22

could be placed close to the q = 1 surface in a variety of conditions by an appropriate choice of frequency without any hinderance from other undesirable ion resonances. The MCD results of this scenario are shown in Fig. 23 (a)-(d). Again refering to Table 1 and Fig. 2, we note that for outboard location, we must phase the antenna such that $\Delta\phi = -90°$ for flattening of the J-profile required for sawtooth stabilization.

6. DISCUSSION AND CONCLUSIONS.

In a scenario, in which the fast-wave power can be dominantly absorbed on one side of the minority cyclotron layer (strong damping case such as possibly in a reactor), minority current drive can be used to drive unidirectional noninductive currents, an idea that was pursued by the earlier authors [6,11]. In such a situation, minority current drive (MCD) efficiency can be augmented by cancelling the effect of background ion rotation (lowering the value of λ in Eq. 9) by injecting a low energy neutral beam of majority particles in a direction dependent upon the antenna phasing and the direction of minority current driven. This could form yet another means of complimentarity between two schemes of heating and current drive.

The control of sawteeth by minority current drive also provides a handle on the energy confinement inside the q = 1 surface and hence on burn control in a reactor. The DD-neutrons produced in the JET minority ion current-drive experiments of sawtooth stabilization and destabilization show that on average DD-neutrons are lower by a factor of 0.6 in the destablized case [39,40]. The results of a model [39] calculation reproduce these results fairly well and predict that by changing the sawtooth period, in ITER-EDA like plasmas, from 3 s to 0.2 s such as that produced by minority ion current drive effects at q = 1 surface, the D-T reactivity of the plasma could be reduced by a factor of 0.75. However, the model is preliminary and the dynamic behaviour of the burn control (delayed response time due to current diffusion) has not been evaluated.

We note further that the experimental results of sawteeth control by minority ion current drive presented in this paper represent an indirect evidence of magnetic shear control in a tokamak. The available diagnostics such as Faraday rotation measurements are unable to resolve the local change in the current density profiles produced in these experiments. However, if the sawteeth behaviour is governed by the internal kink stability model assumed in this paper, the qualitative agreement obtained between the experimental sawtooth period and that obtained with the full simulation using the minority current drive calculation and the above stability theory indicates that, indeed, a shear control is being achieved. Further confidence in these assertions will be obtained if the forthcoming MCD shear reversal experiments in JET

also lead to improved confinement such as that in PEP + H-modes assuming that the latter are the result of shear reversal.

In conclusion, experimental evidence of sawtooth stabilization and destabilization using fast wave minority current drive in JET has been presented. The sawtooth control is accomplished by locating the minority cyclotron layer (R_{CH}) close to the q = 1 surface inboard and launching only a modest amount of RF power (5 MW) in JET with a current drive phasing $\Delta\phi = +90°$ or $-90°$ between the current straps. This leads to a dipolar current driven across the q = 1 surface thus changing the gradient of the current density (J), the safety factor (q) and the shear (r/q dq/dr) at this location. A model of the fast-wave current drive describing simultaneously the e-TTMP and the minority current drive based on earlier theories is developed and integrated into a ray tracing code to determine driven current density profiles. These are then coupled to internal kink stability analysis code to determine the sawtooth period. A full simulation of a stabilized sawtooth discharge in the MCD scenario shows qualitatively a good agreement with the experimentally observed sawtooth period. The sawtooth instability threshold is dependent on several paremeters that are not accurately known and at best can only be estimated approximately. Further, the nature of the sawtooth instability is such that both in experiments and in simulations, the actual sawtooth period can be somewhat different without any apparent change in the external parameters that are under the control of an experimentalist.

It has been shown that the MCD can also be used to produce strong shear reversal well within the q = 1 surface for long duration high confinement regimes similar to the ones obtained by deep pellet injection scenarios in JET. Further, the analysis of the minority current drive shows that net MCD normalized efficiency depends on the background plasma response and H-minority in a D or D-T plasma can be used effectively for sawtooth control whereas (He3)-D scenario is found to have poor MCD efficiency. Our MCD model takes into account the effect of electron and ion trapping but the effect of actual transfer of minority ions from non trapped to trapped regions and the resulting increase cancellation of the minority current (Ohkawa effect) is not included.

ACKNOWLEDGEMENT.

batch processing of the soft X-ray data and in the current drive computational work is gratefully acknowledged.

REFERENCES.

[1] REBUT P.H. et al., Proc. 12th IAEA Conf., Nice, France, 2 (1989) 191.

[2] HUGON, M. et al., Nuclear Fusion, 32 (1992) 33.

[3] START, D.F.H. et al., Proc. 19th EPS Conf. Innsbruck, 16C (1992) part II, 897

[4] FISCH, N.J., Rev. Modern Phys, 59 (1987) 175.

[5] BHATNAGAR, V.P. et al., Proc. Int. Theory Workshop, Varenna, Italy, (1990) 243.

[6] FISCH, N.J., Nuclear Fusion, 21 (1981) 15.

[7] PORCELLI, F. et al., Proc. 19th EPS Conf.,Innsbruck, 16C (1992) part II, 901.

[8] BHATNAGAR, V.P. et al., Nuclear Fusion 24 (1984) 995.

[9] EHST, D. et al., Nuclear Fusion, 31 (1991) 1933.

[10] STIX, T.H., Nuclear Fusion, 22 (1975) 737.

[11] CHIU, S.C. et al., Nuclear Fusion, 23 (1983) 499.

[12] OHKAWA, T., Nucl Fusion, 10 (1970) 185.

[13] BHATNAGAR, V.P. et al., Nuclear Fusion 22 (1982) 280.

[14] BRAMBILLA, M., Report IPP 4/210 (1983), Max Planck Institute, Garching, Germany.

[15] GOULDING, R. et al., Proc. 15th Symp. on Fus. Eng., Hyannis, Mass., (U.S.A.) October 1993.

[16] CHIU, S.C., et al., Nuclear Fusion 22 (1989) 2175.

[17] KARNEY, C.F.F. et al., in Applications of Radiofrequency Power to Plasma (Proc. 8th Topical Conf. Irvine, 1989), McWilliams, R., AIP, N.Y. (1989) 430.

[18] CONNOR, J.W., CORDEY, J.G., Nucl Fusion, 14 (1974) 185.

[19] TRUBINIKOV, B.A., in Reviews of Plasma Physics, (LEONTOVICH, M.A., Ed.), Consultants Bureau, New York, vol. 1 (1965) 105.

[20] COPPI, B. et al., Fiz. Plasmy, 6 (1976) 961, see transaltion in Sov. J. of Plasma Physics

[21] MIGLIULIO, S., PEGORARO, S., PORCELLI, F., Phys. Fluids, B3 (1991) 1938.

[22] LAZZARO, E., MANTICA, P., 'Experimental Identification of Tokamak Equilibrium using Magnetic and Diamagnetic Signals', Report JET-P(87)58, JET Joint Undertaking, Abingdon, England (unpublished).

[23] CENACCHI, G. and TARONI, A., 'A Transport Code at JET', Report JET-IR(88)03, JET Joint Undertaking, Abingdon, England (unpublished).

[24] PORCELLI, F. et al., 'Sawtooth Instability With q On-Axis Below Unity', Report JET-IR(88)16, JET Joint Undertaking, Abingdon, England (unpublished).

[25] CONNOR, J.W., HASTIE, R.J., Report CLM-M106, 1985, Culham Laboratory, Culham, OXON (U.K.)

[26] PORCELLI, F., CHERUBINI, A., BHATNAGAR, V.P., JACQUINOT, J., START, D.F.H., 'Sawtooth Stability and Control', under preparation

[27] REBUT, P-H., LALLIA, P.P., WATKINS, M.L., in Plasma Phys and Contr. Nuclear Fusion Research 1988 (Proc. 12th Int. Conf., Nice, 1988), vol. 2, IAEA, Vienna (1989) 191.

[28] WADE, T.J., JACQUINOT, J., BOSIA, G., et al., (Proc. 14 Symp. Fusion Engg, San Diego, 1991) Vol. 1, IEEE Nuclear Physical Society, (1991) 902.

[29] KAYE A.S., JACQUINOT, J., LALLIA, P., WADE, T.J., Fusion Technology, 11 (1987) 203.

[30] BOSIA, G., JACQUINOT, J., Proc. IAEA Tech. Comm. Meeting on Fast Wave Current Drive in Reactor Scale Tokamaks, Arles, France, Eds. MOREAU D., BECOULET, A., PEYSSON Y. (1991) 471.

[31] WALKER, C.I., BRINKSCHULTE, H., BURES, M., et al., (Proc. 15th Symp. Fusion Techno, Utrecht, Holland, 1988) Elsevier Science Publishers B.V., Vol. 1, (1989) 444.

[32] ORLINSKIJ, D.V. and MAGYAR G., Nuclear Fusion, 28 (1988) 611.

[33] EDWARDS A.W., FAHRBACH, H.W., Gill, R.D., GRANAETZ, R. et al., Rev. of Scientific Instruments, 57 (1986) 2142.

[34] BRAITHWATE, G. et al., The Rev. of Scientific Instruments, 60 (1989) 2835.

[35] BHATNAGAR, V.P., Tech. Note JET-JDN/J87.4, JET Joint Undertaking, Abingdon (U.K.).

[36] CHALAND, F. and BHATNAGAR, V.P., Report JET-R(93)06, JET Joint Undertaking, Abingdon (U.K.).

[37] CAMPBELL D.J., et al., Phys Rev. Lett., 60 (1988) 2148.

[38] BHATNAGAR, V.P., BOSIA, G., JACQUINOT, J., PORCELLI, F., Proc. 20th EPS Conf. on Contr. Fus. and Plasma Phys, Lisbon, 17C (1993), part III, 937.

[39]. START, D.F.H., ERIKSSON, L., "Burn Control in a Reactor by Minority Current Drive Effects on Sawteeth", (1993), JET Joint Undertaking, Abingdon, private communication.

[40]. BHATNAGAR, V.P., JACQUINOT, J. (Eds), 'Fast Wave Heating and Current Drive in ITER', NET Report 103, EUR-FU/XII/163/94 (1994), The NET Team, Garching, Germany

Table 1. Expected Effects on Current Density (J) and safety factor (q) profiles due to e-TTMP and MCD.

Δφ (Deg)	Wave Direction	Position of R_c	Sign of TTMP CD	SIGN OF MCD		CURRENT DENSITY GRAD at R_c	SAFETY FACTOR q		Minority Trapping (Lower/Higher)
				HFS of R_c	LFS of R_c		at R_c	at centre	
+90	ACW	Inboard	+Ve	+Ve	-Ve	flatten	flatten	decrease	L
+90	ACW	Outboard	+Ve	+Ve	-Ve	steepen	steepen	decrease	H
-90	CW	Inboard	-Ve	-Ve	+Ve	steepen	steepen	increase	L
-90	CW	Outboard	-Ve	-Ve	+Ve	flatten	flatten	increase	H

Assume Plasma Current : Clockwise (+Ve)
B_ϕ = ACW (anti-clockwise)

Table 2 Plasma and antenna parameters used in the three calculations.

PLASMA PARAMETERS

		JET (A1)	JET (A2)	ITER (EDA)
Plasma composition		(H)-D	(H)-D	(H)-D-T
Minority concentration	n_{min}/n_e	0.14	0.22	0.018
Z-effective		1.66	1.66	1.15
Toroidal field on axis	$B_0(T)$	2.62	3	6
Plasma Current	$I_P(MA)$	2.05	2	25
Operation frequency	$f(MHz)$	42.7	47	74
Central Electron Temperature	$T_{e0}(keV)$	6.25	6	19
Central ion Temperature	$T_{i0}(keV)$	5.6	5	19
Temperature profile exponent	p	2	1.5	1
Central plasma density	$n_{e0}(10^{19}m^{-3})$	2.6	3	14
Edge plasma density	$n_{es}(10^{19}m^{-3})$	0.28	0.6	8
Density profile exponent	ρ	0.6	0.6	0.26
Torus major radius	$R_0(m)$	2.96	2.96	7.75
Plasma radius	$a_p(m)$	0.98	0.95	2.8
Elongation	κ	1.35	1.4	1.6
Triangularity	δ	0.02	0.03	0.25
Shafranov shift	$\Delta_0(m)$	0.14	0.14	0.5

ANTENNA PARAMETERS

Antenna conductor to limiter distance	$a(m)$	0.04	0.08	0.12
Antenna conductor to backwall distance	$d(m)$	0.1	0.25	0.3
Antenna conductor to screen distance	$x_{sc}(m)$	0.012	0.012	0.05
Length of one antenna element	w_y (m)	0.8	0.8	2.6
Half-width of the antenna element	$w_z(m)$	0.055	0.105	0.125
number of boxes energized	N_{box}	8	4	36
Number of antenna per box	N_y, N_z	2,2	2,4	1,1
Mid-line distance between two conductors	$L_z(m)$	0.31	0.4	0.466
Phase between successive straps	$\Delta\phi(°)$	90	90	-90

Table 3. Critical Energy and MCD efficiency factor $\eta(Z,m)$ for Several Minority CD Scenarios.

Scenario	Z_h	m_h	Z_i	m_i	E_C/T_e	$\eta(Z,m)$
(H)-D	1	1	1	1	~ 10	0.76
(H)-He3	1	1	2	3	~ 12.5	0.52
(D)-T	1	2	1	3	~ 15	1.13
(He3)-D	2	3	1	2	~ 30	0.56
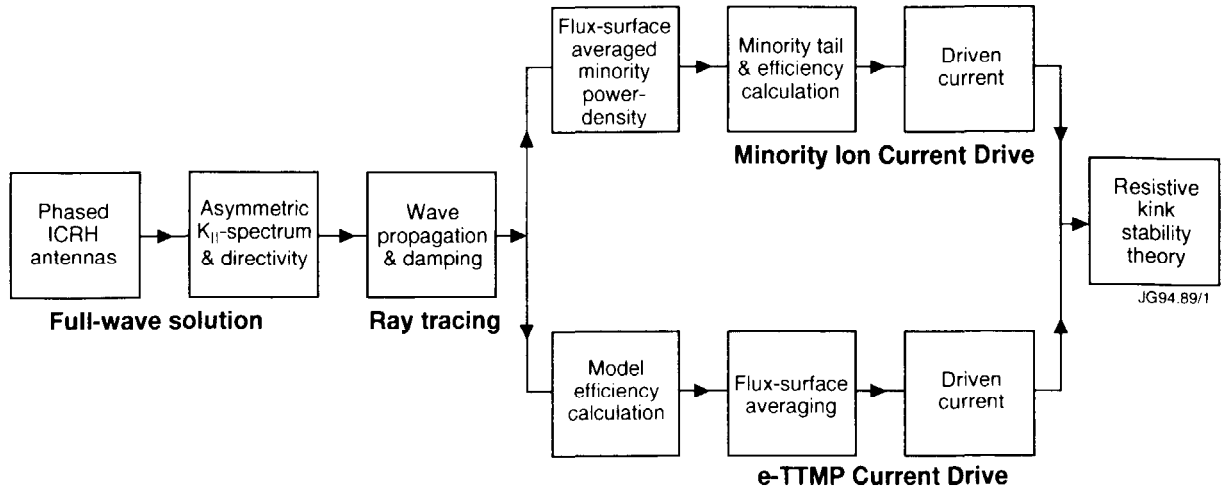
FIG. 1. A schematic block diagram showing the layout of various codes used in the fast wave current drive calculations and sawtooth stabilization.
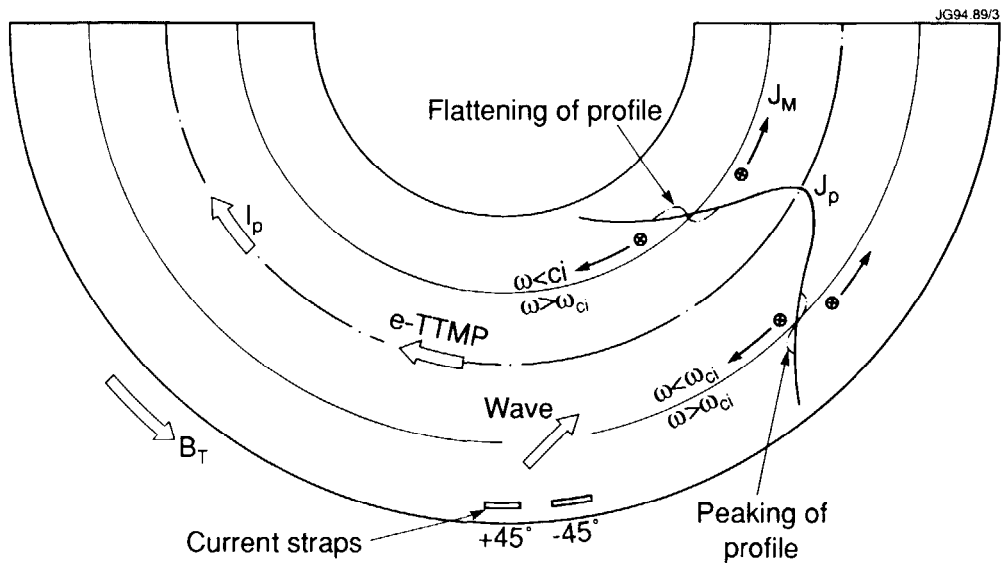
FIG. 2. A schematic diagram showing the directions of the e-TTMP and minority current drive at inboard and outboard locations of the cyclotron layer when $\Delta\phi = +90°$ and I_p and B_ϕ are as shown. Reversing the phase reverses the sign of all currents shown.
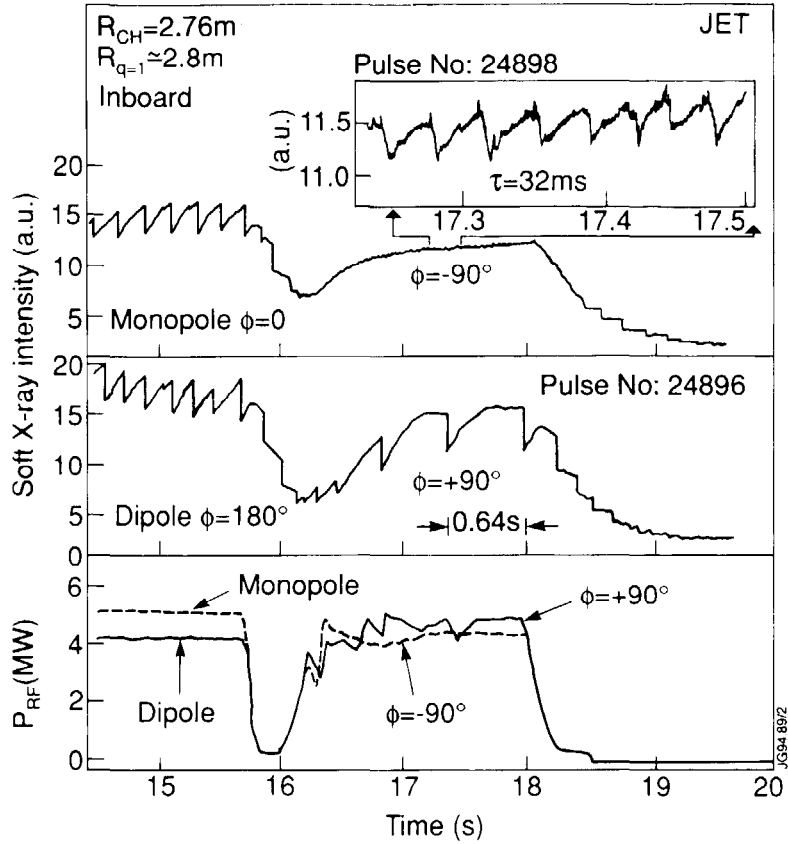
FIG. 3. The difference in sawtooth behaviour as measured by the soft X-ray diagnostic under minority current drive near q = 1 surface on the high field side under a $\Delta\phi$ = 0, 180°, +90°, −90°-phased JET A1-antennas. Sawtooth stabilization and destabilzation is seen for $\Delta\phi$ = + 90° and −90° respectively. The inset shows the detail of destabilized sawteeth.
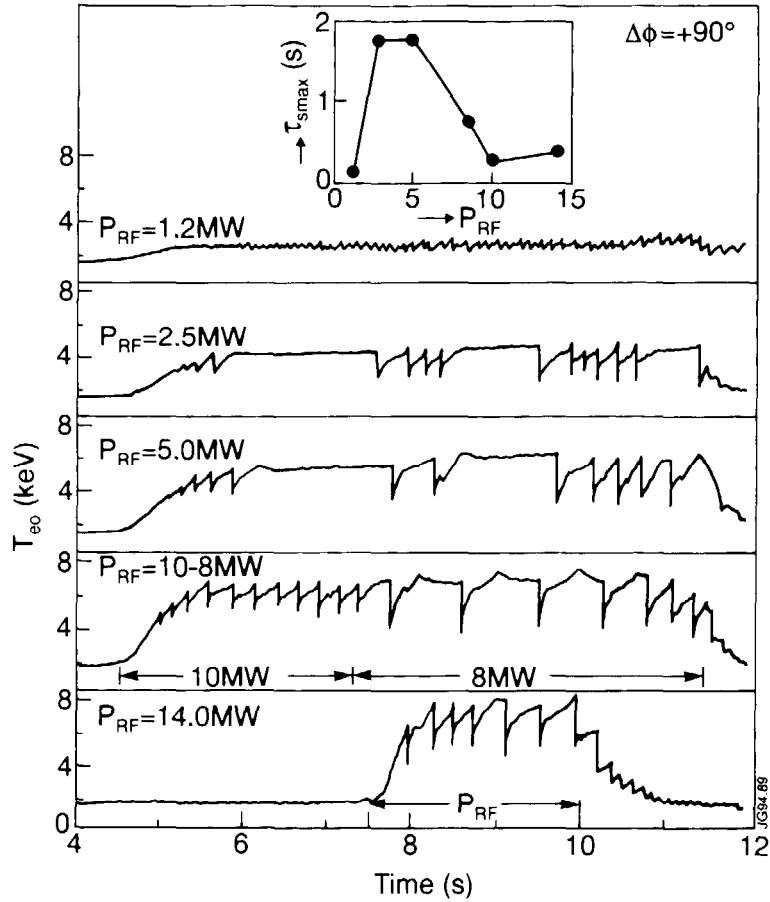
FIG. 4. Time traces of central electron temperature measured by ECE for several different RF power levels showing the behaviour of sawtooth period under minority current drive near the inboard q = 1 surface with $\Delta\phi = +90°$ The inset shows the maximum sawtooth period as a function of RF power.

Pulse No: 27190
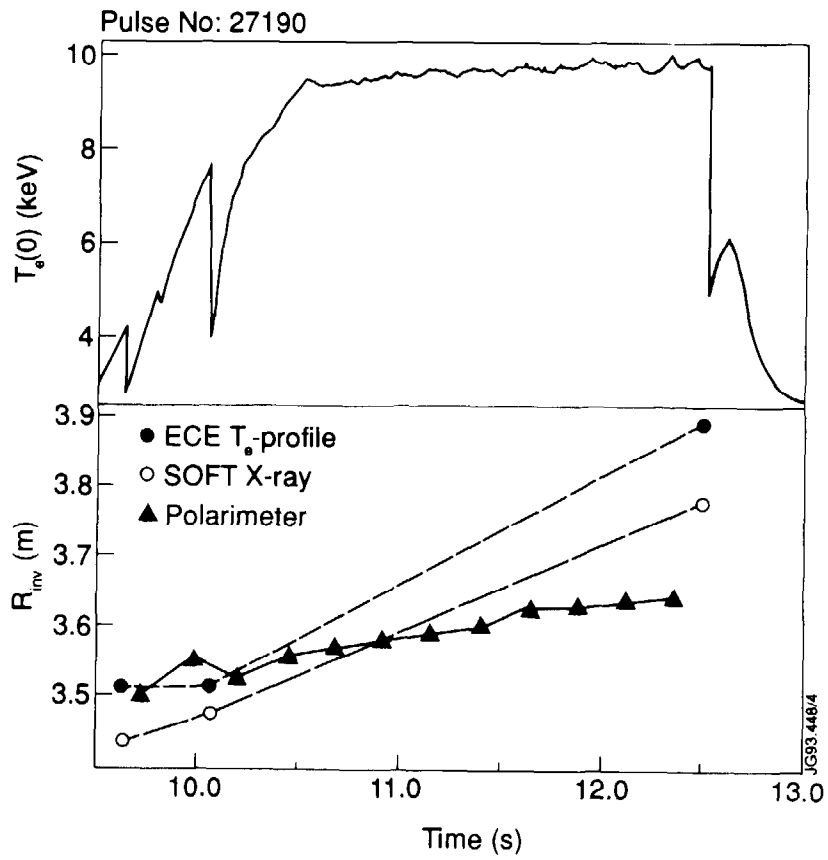
FIG. 5. The time evolution of the inboard inversion radius (approximately $q = 1$ surface) measured by three different diagnostics (ECE, Soft X-ray and Faraday rotation polarimeter) during a monster sawtooth produced by central ICRF heating. The trace in the upper box is the T_{e0} measured by ECE.
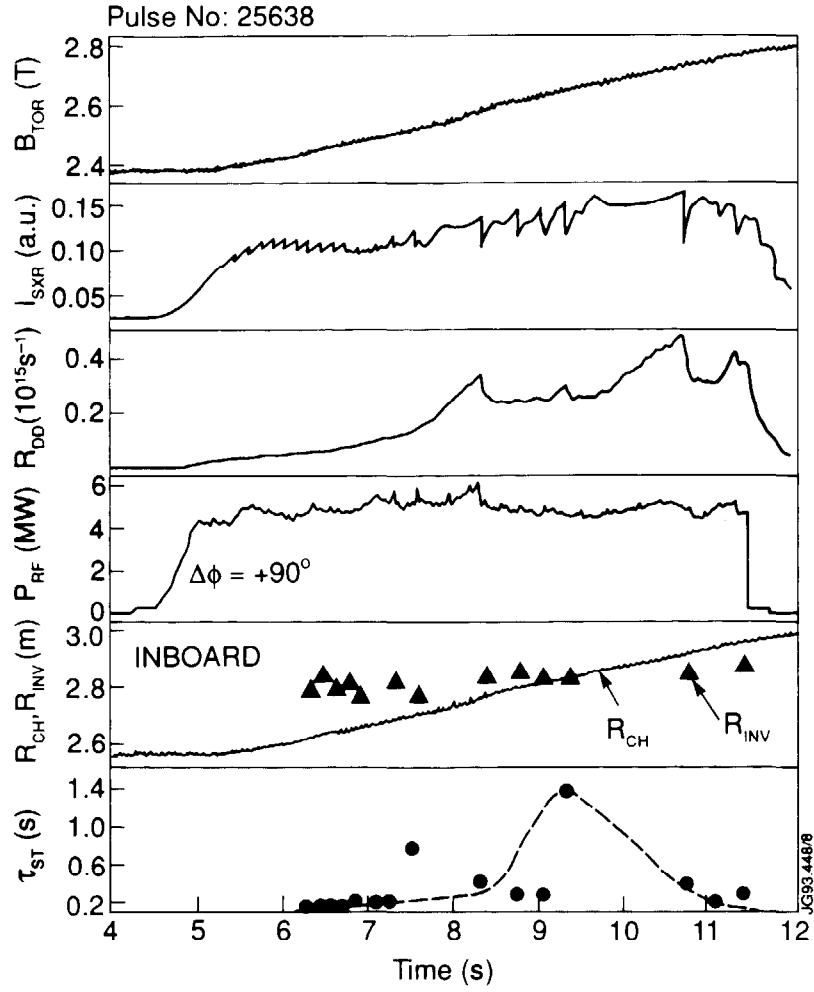
FIG. 6. Time traces of toroidal field (B_{TOR}) ramp up, soft X-ray intensity (I_{SXR}), D-D reaction rate (R_{DD}), RF power (P_{RF}) and hydrogen cyclotron layer (R_{CH}). The solid triangles and solid circles respectively represent the inversion radius and the sawtooth period observed which is maximum when $R_{CH} \cong R_{INV}$ inboard with $\Delta\phi = + 90°$.
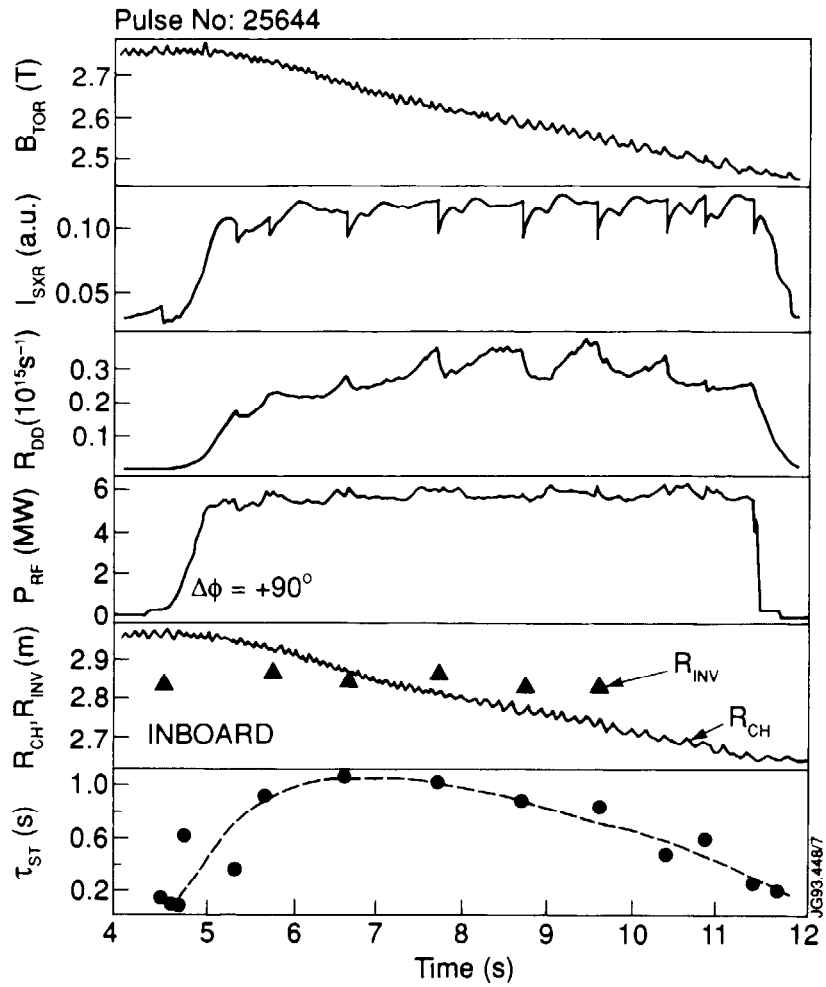
FIG. 7. Same as in Fig. 6 except now during an experiment with B_{TOR} ramp down.
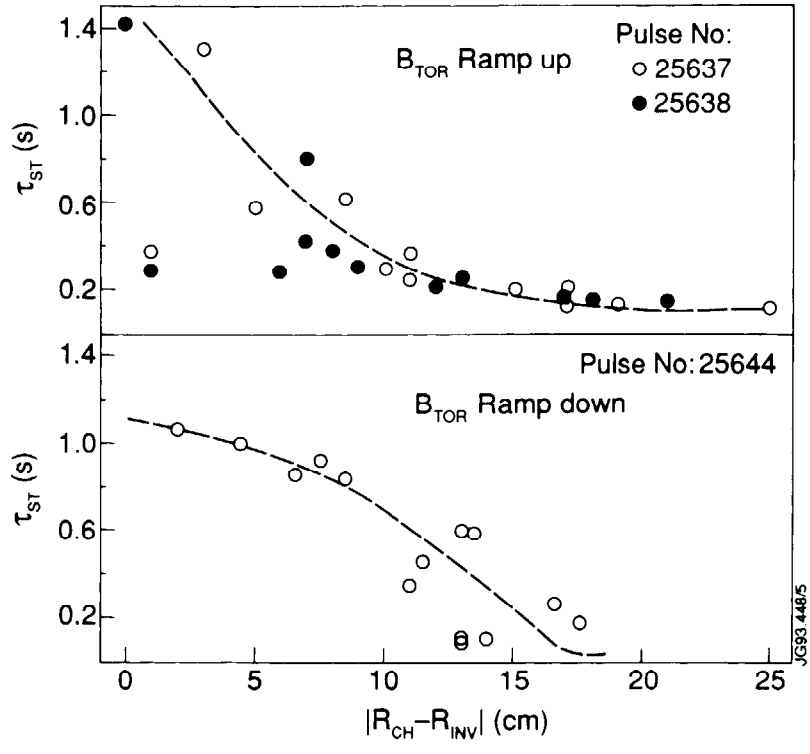
FIG. 8. Sawtooth period deduced from soft X-ray signal is plotted as a function of the magnitude of the distance between R_{CH} and R_{INV} in B_{TOR} ramp up and ramp down experiments under minority current drive inboard with $\Delta\phi = +90°$.
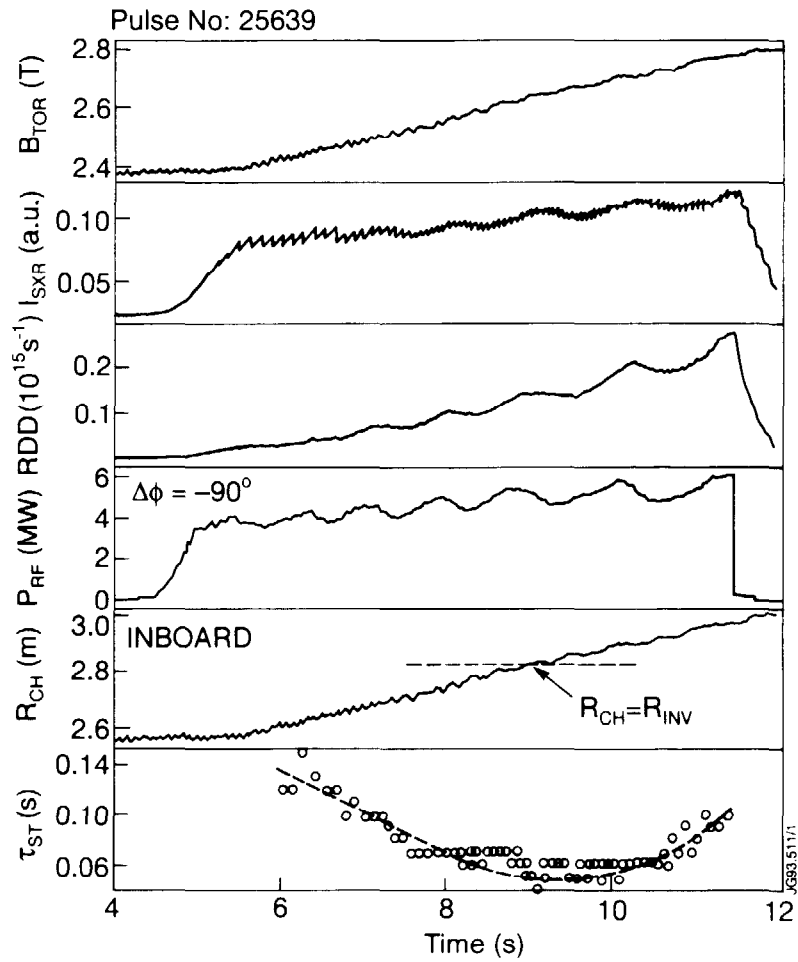
FIG. 9. Same as Fig. 6 but with $\Delta\phi = -90°$. The sawteeth are well destabilised when R_{CH} is close to R_{INV}.
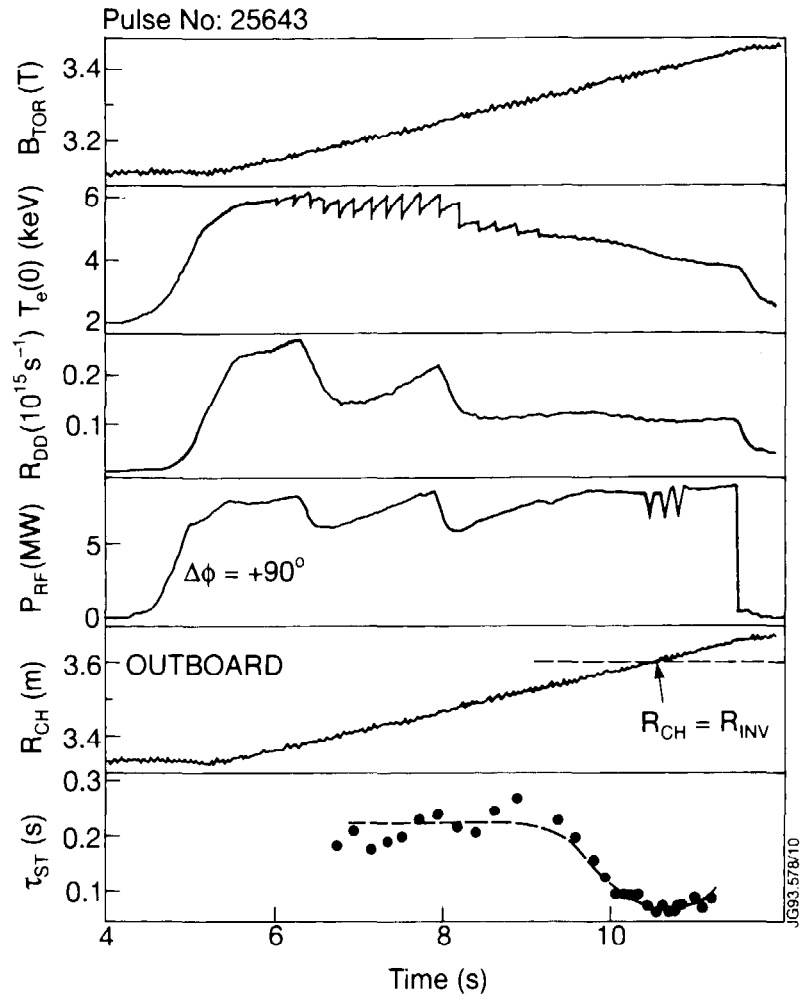
FIG. 10. Same as Fig. 8 but with $\Delta\phi = +90°$ and R_{CH} is close to R_{INV} on the outboard. The minority current drive leads to a destabilization of sawteeth.
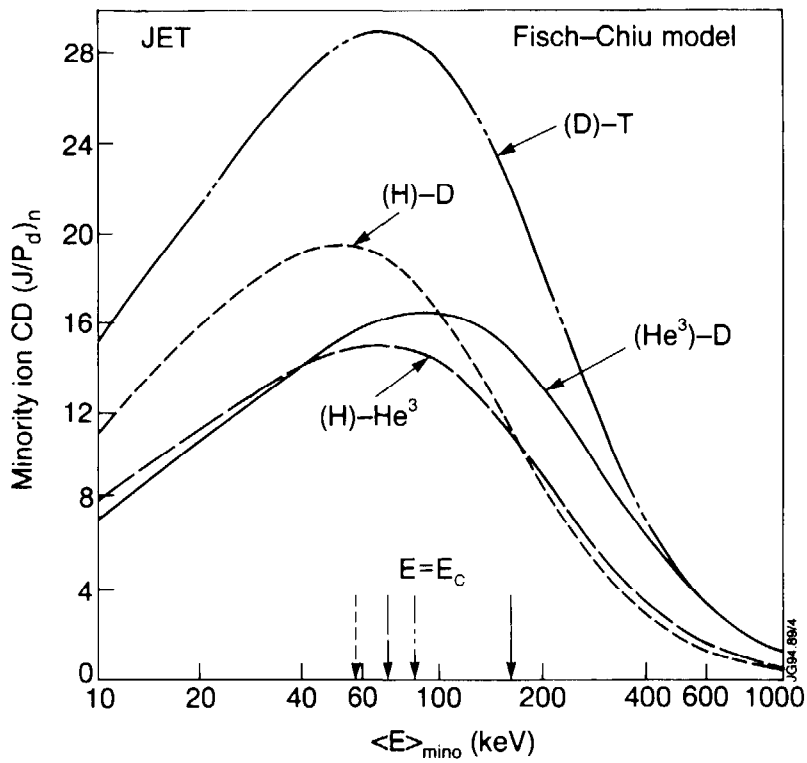
FIG. 11. Minority ion current drive normalized efficiency factor is plotted as a function of minority ion average energy calculated by the Stix model for several scenarios. These results do not include the background species response for which see Fig. 12. Minority ion symbol is enclosed in parenthesis. The vertical arrows on the abcissae indicate roughly the critical energy for each scenario.
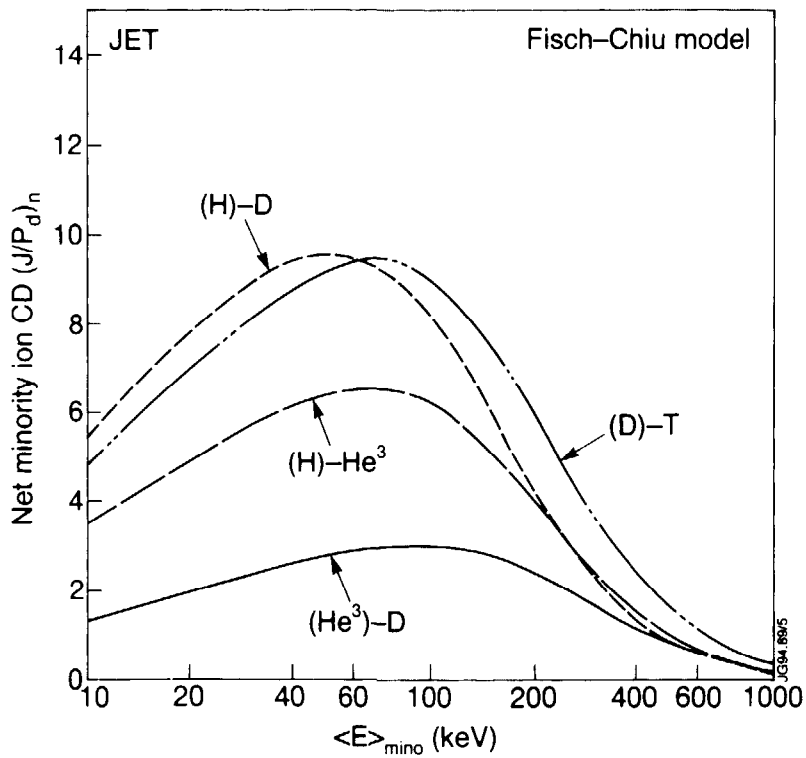
FIG. 12. Same as in Fig. 11 except now the net minority ion current drive normalized efficiency factor is plotted which takes account of the response of the background species.
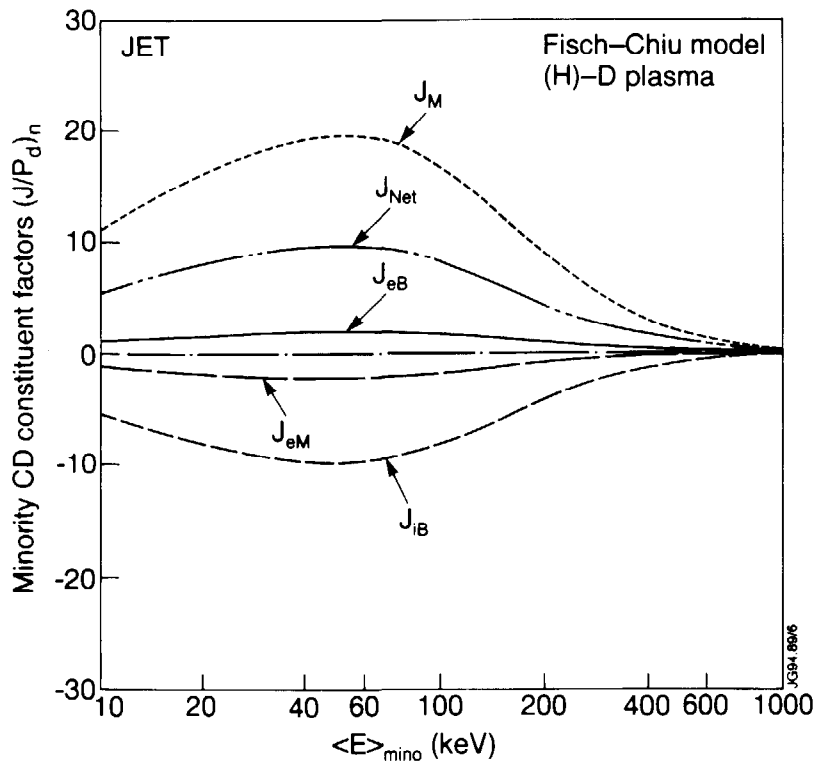
FIG. 13. Same as in Fig. 12 showing the details of all the minority current drive constituent factors for (H)-D scenario. J_M is minority CD, J_{eB} is due to electrons dragged by the backgound ions, J_{eM} is due to electrons dragged by the minority ions, J_{iB} is due to background ion roatation. J_{Net} is the algebraic sum of all the above factors.
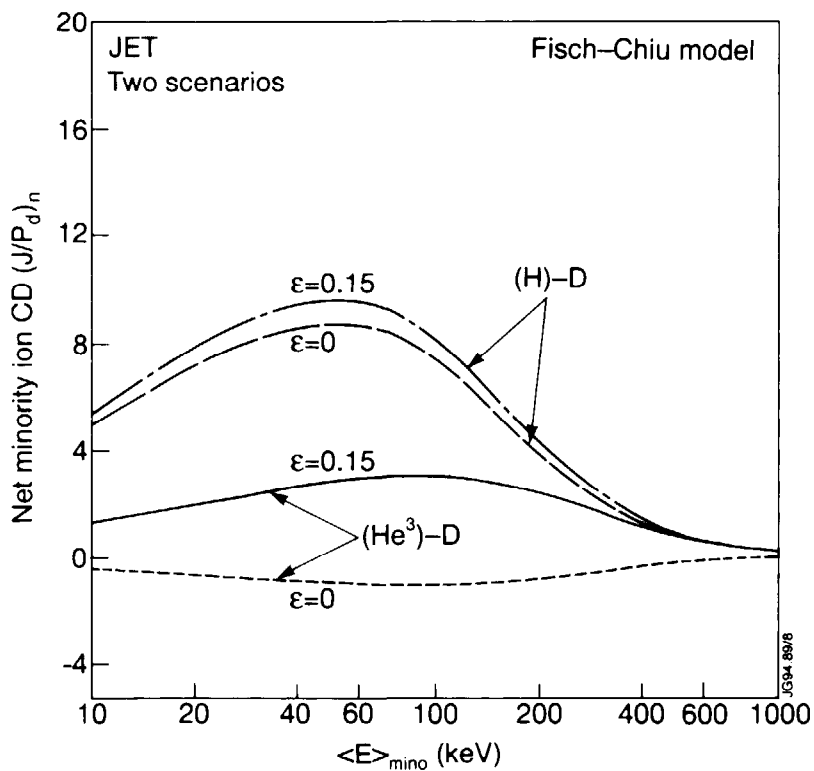
FIG. 14. Net normalized minority current drive factor as a function of minority average energy for two values of inverse aspect ratio $\varepsilon = 0$ and 0.15 for (H)-D and (He3)-D scenarios. For $\varepsilon = 0$, J_{Net} can even become negative in (He3)-D scenario.
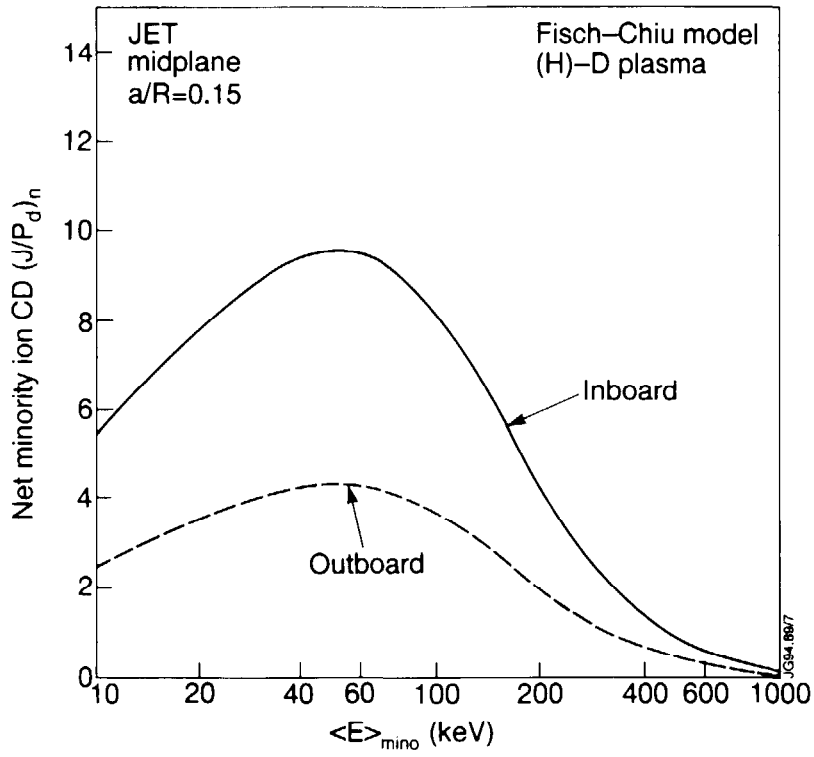
FIG. 15. Net normalized minority current drive factor as a function of minority average energy at inboard and outboard locations at $\varepsilon = 0.15$ in (H)-D plasma showing the effect of minority ion trapping. Note that the Ohkawa effect is not included here.
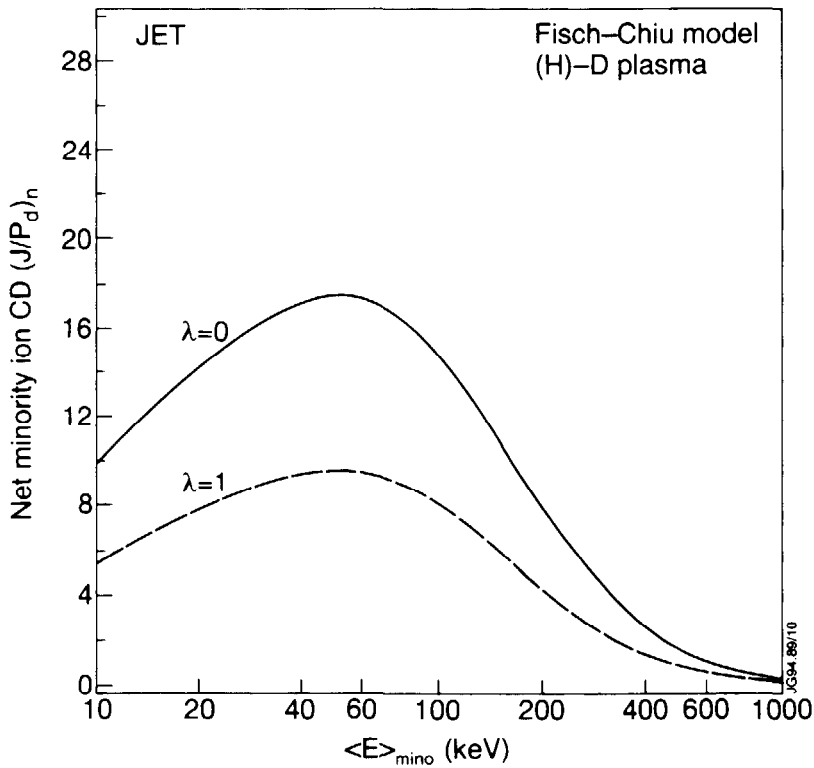
FIG. 16. Same as in Fig. 15 with the effect of background ion rotation ($\lambda = 1$) and without ($\lambda = 0$).
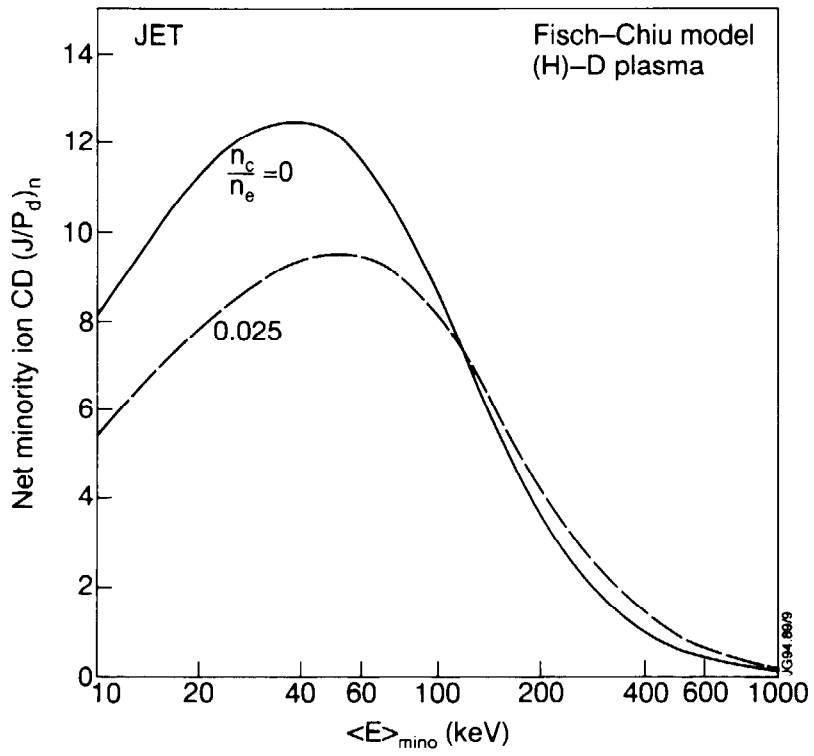
FIG. 17. Same as in Fig. 16 with and without a small impurity ion (carbon) concentration.
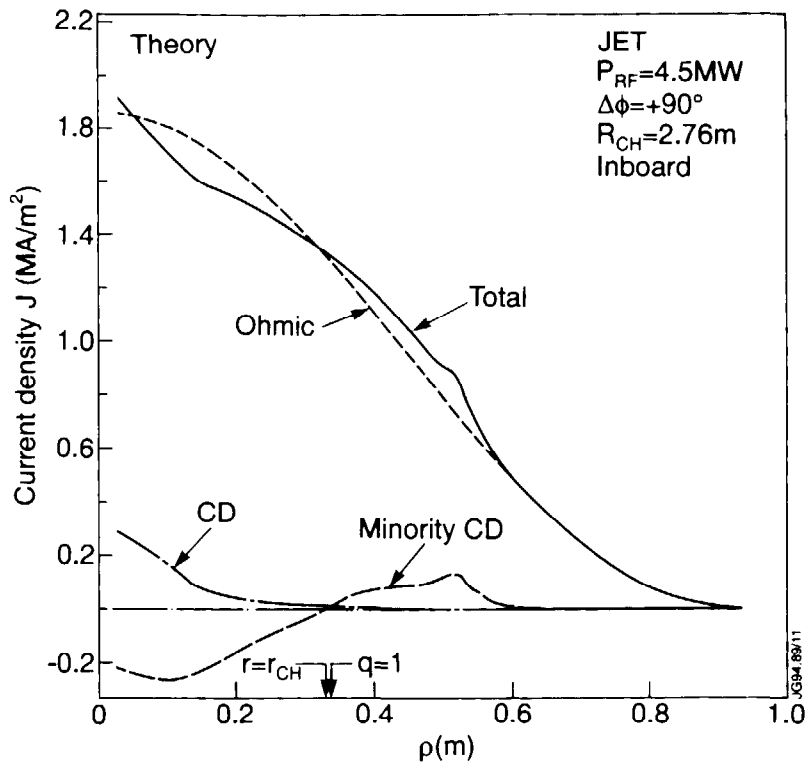
FIG. 18(a). The e-TTMP, minority, ohmic and the total current density as a function of the minor radius in JET calculated for the parameters of shot 24896 (see Table 2, case: JET-A1) when the R_{CH} is located close to the $q = 1$ surface on the HFS and $\Delta\phi = +90°$. This leads to flattening of J profile at the $q = 1$ surface.
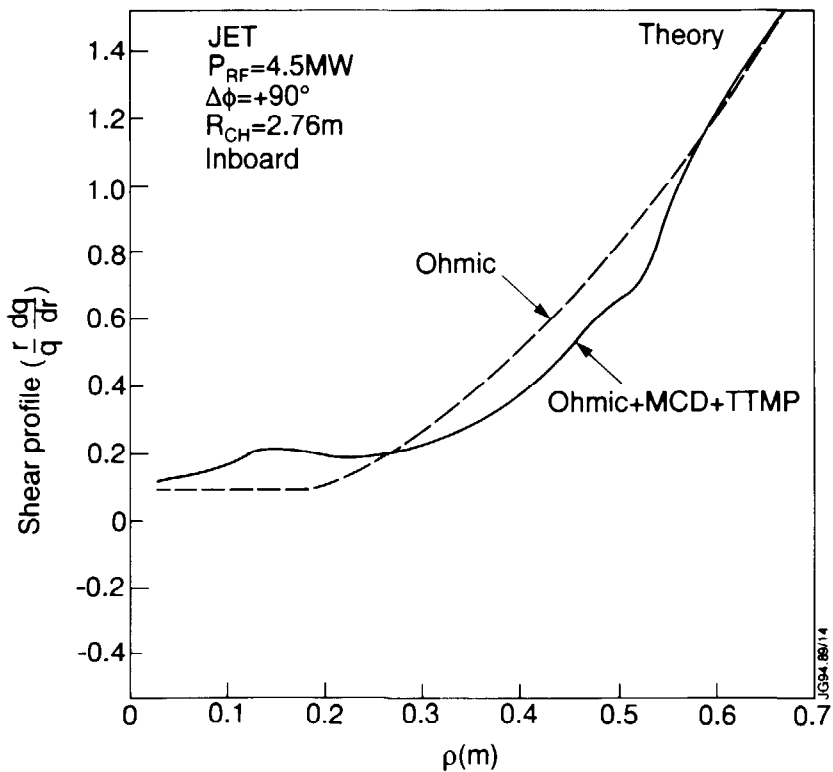
FIG. 18 (b). The magnetic shear profiles for the case of Fig. 18 (a) showing the reduction of shear at the $q = 1$ surface.
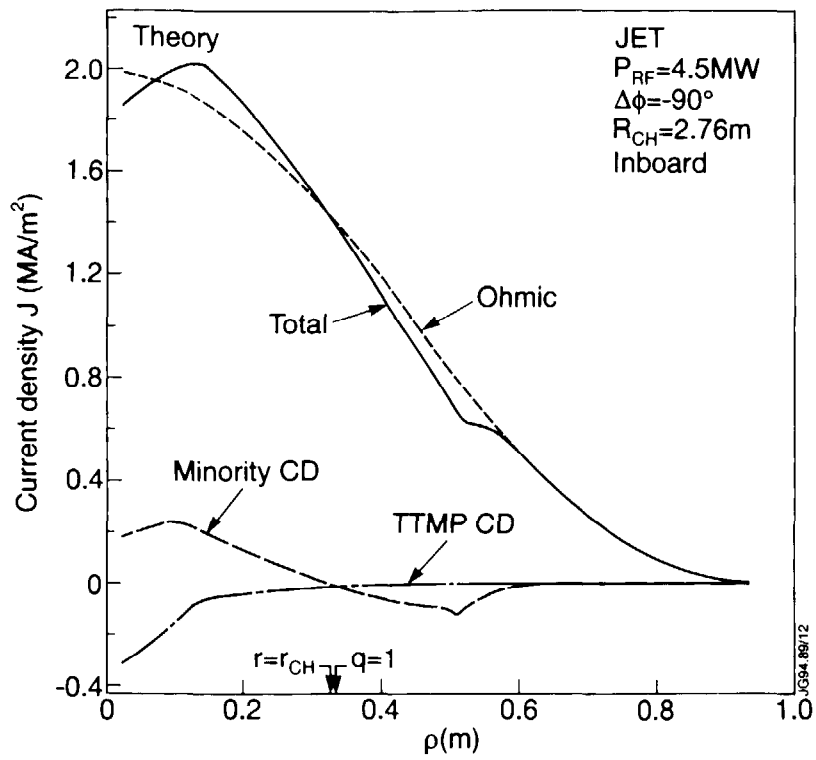
FIG. 19 (a). Same as Fig. 18 (a) but for $\Delta\phi = -90°$ showing the steepening the J-profile at the $q = 1$ surface inboard.
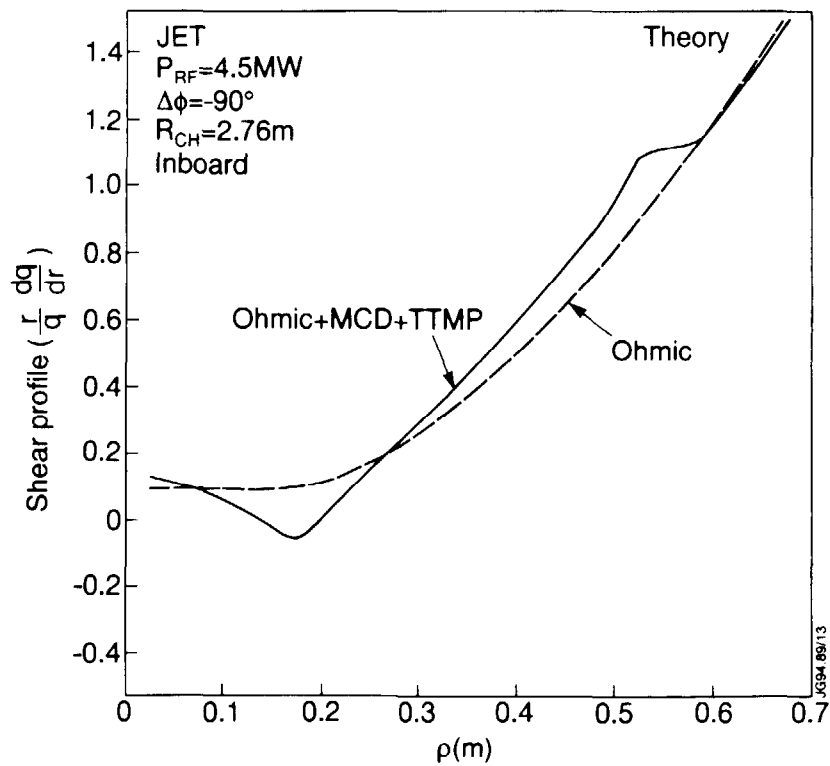
FIG. 19 (b). Same as Fig. 18 (b) but for $\Delta\phi = -90°$ showing an increase in the shear at the $q = 1$ surface inboard.
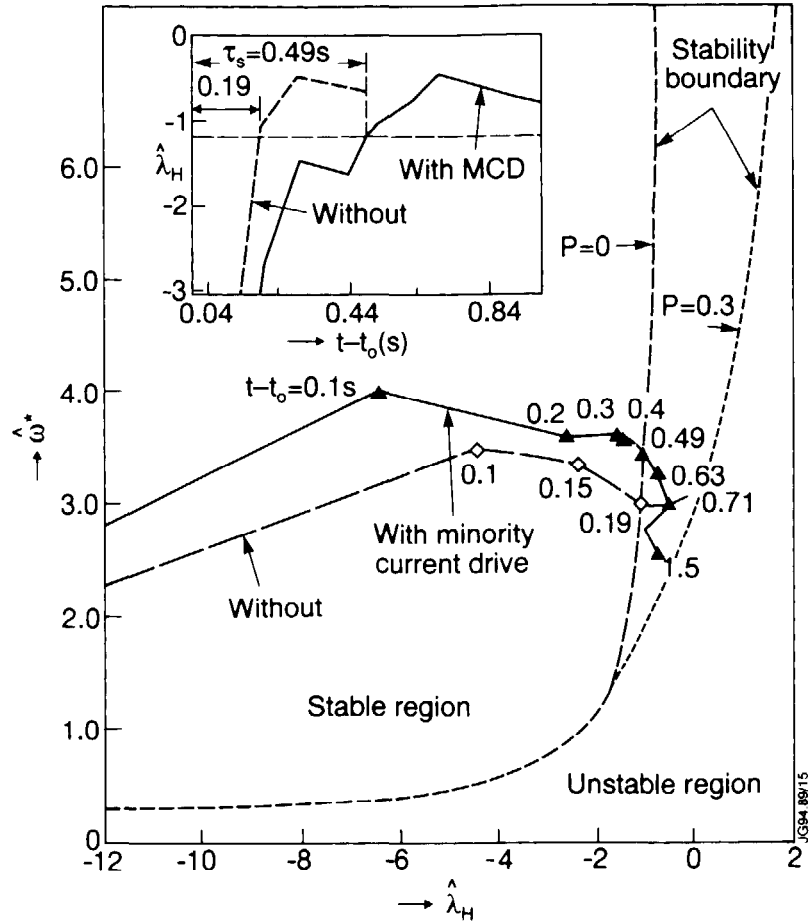
FIG. 20. A plot of the time trajectory of the discharge 24896 in the $(\hat{\omega}^*, \hat{\lambda}_H)$ stability plane with and without minority current drive. Stability boundary for the viscosity parameter P = 0 and P = 0.3 are shown. P = 0.12 is more typical for the JET discharges. The parameter $t - t_0$ represents the time from the bottom of the sawtooth crash. The inset shows the stability parameter $\hat{\lambda}_H$ as a function of time for the same shot where the stability boundary is shown by the horizontal broken line. With MCD, $\tau_s = 0.49$s which is to be compared with the experimental value of 0.64 s (Fig. 3).
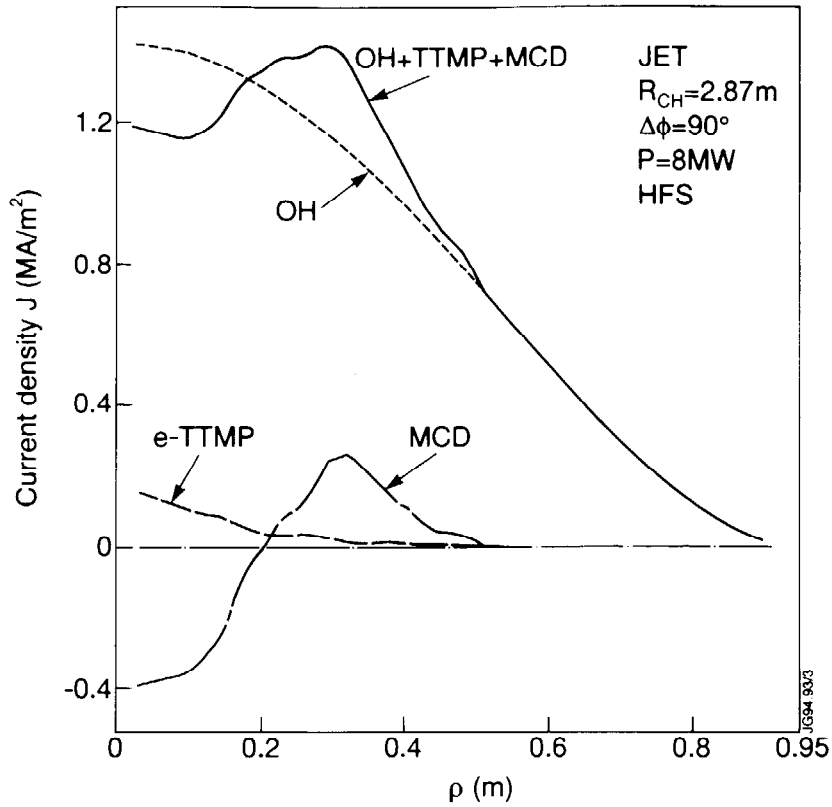
FIG. 21(a). The e-TTMP, minority, ohmic and the total current density as a function of the minor radius for a proposed JET high confinement shear reversed (see Fig. 21 (c)) scenario. For parameters see Table 2, case: JET-A2.
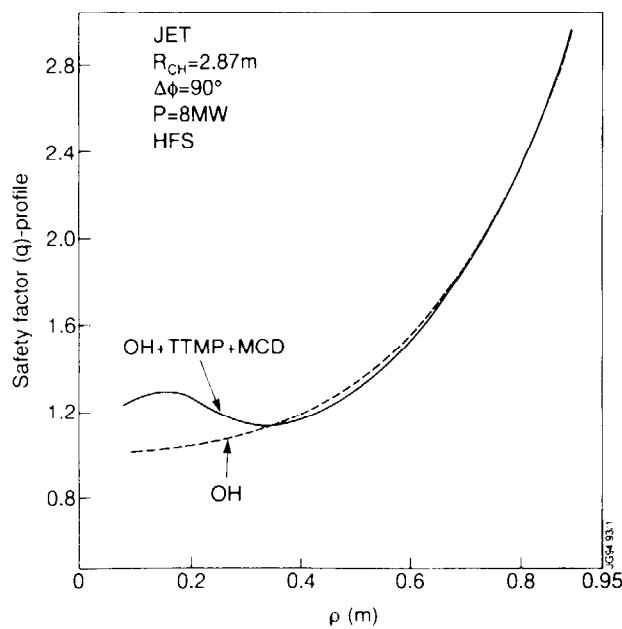

FIG. 21(b). The safety factor profile for the case of Fig. 21 (a) showing the nonmonotonic behaviour of the q-profile.
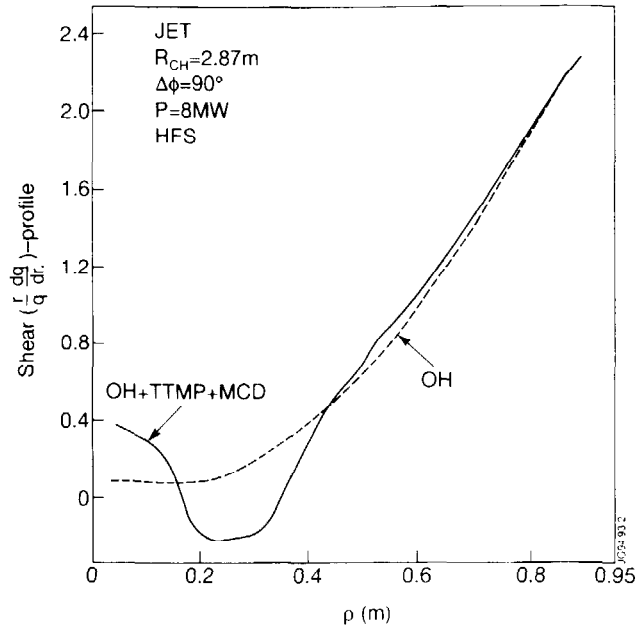
FIG. 21(c). The shear profile for the case of Fig. 21 (a) showing the strong shear inversion.
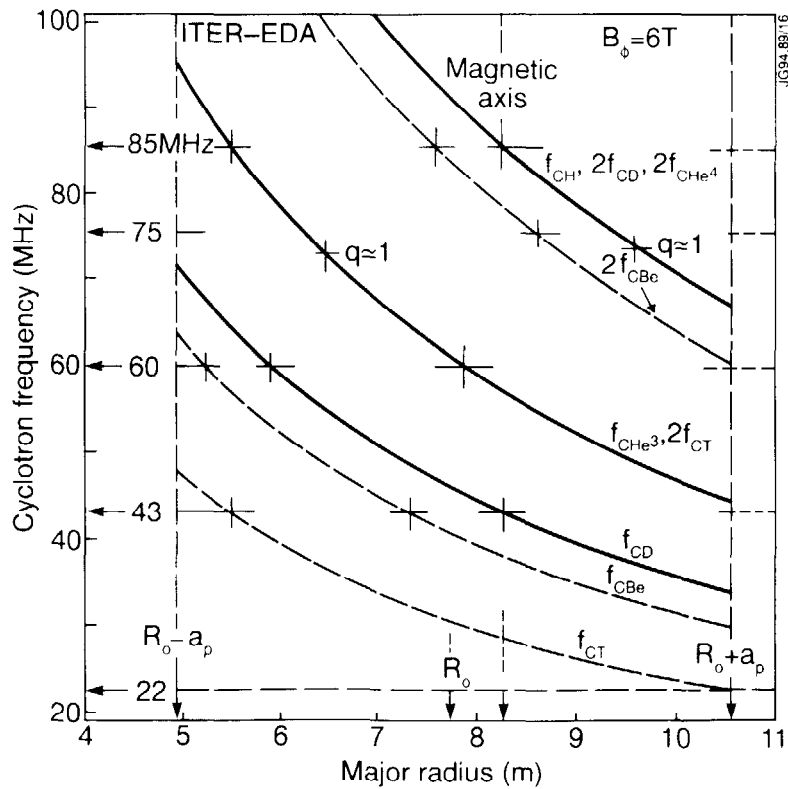

FIG. 22. Fundamnetal and second harmonic ion cyclotron frequencies in ITER-EDA for several plasma species are plotted as a function of major radius for a vacuum field $B_\phi = 6$ T. Frequencies of the main ICRF heating and current drive scenarios are shown together with the approximate locations of $q = 1$ surfaces inboard and outboard.
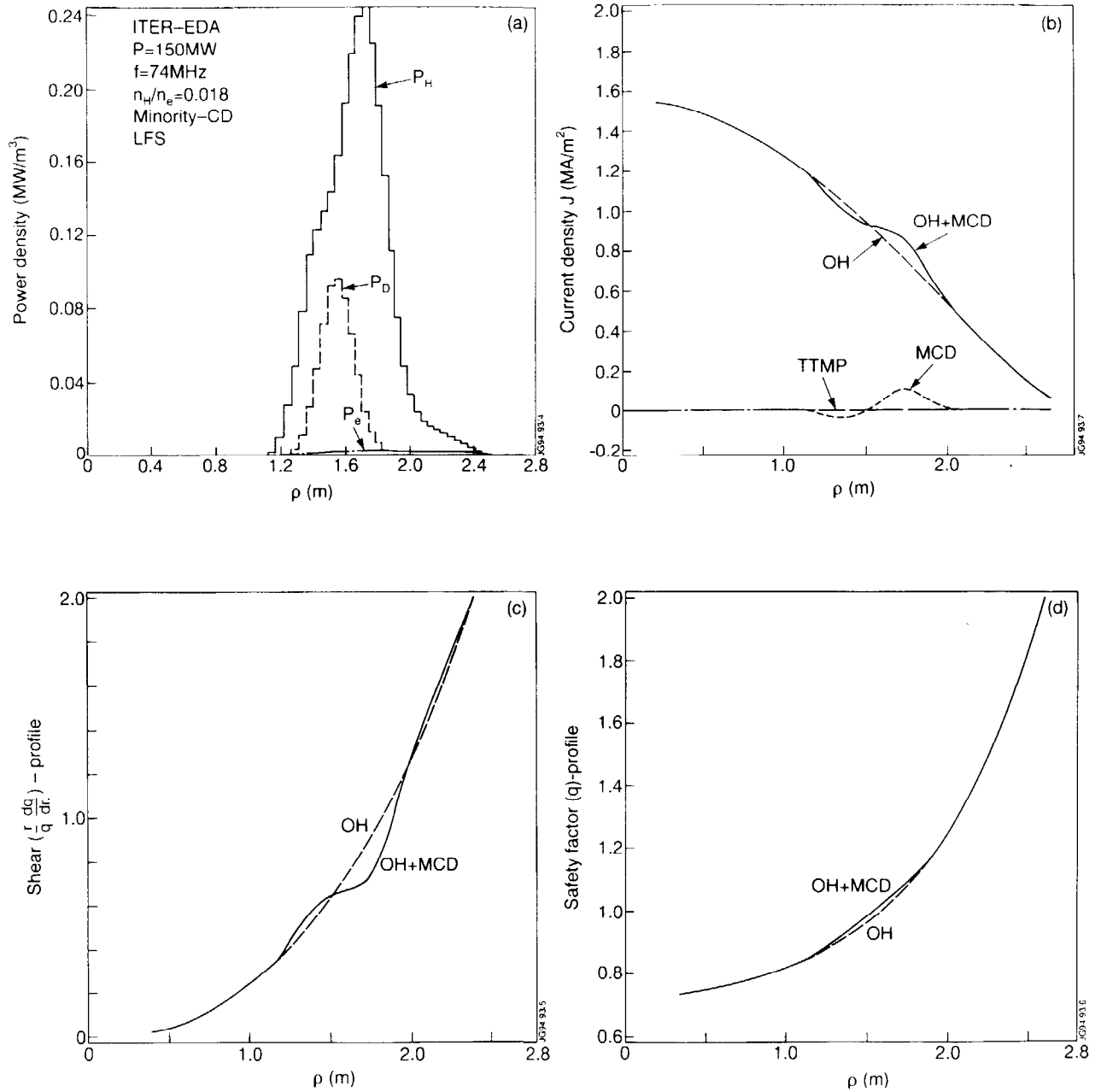
FIG. 23. A minority current drive scenario for sawtooth control in ITER-EDA (H)-D-T plasma (see Table 2, case: ITER-EDA): (a) Power deposition profile, (b) Current density profile, (c) Shear profile and (d) Safety factor profile. All the above have been plotted with and without minority current drive.